PRACTICAL SUPERCONDUCTOR DEVELOPMENT FOR ELECTRICAL POWER APPLICATIONS ARGONNE NATIONAL LABORATORY QUARTERLY REPORT FOR THE PERIOD ENDING SEPTEMBER 30, 2000

This is a multiyear experimental research program focused on improving relevant material properties of high-T_c superconductors (HTSs) and on development of fabrication methods that can be transferred to industry for production of commercial conductors. The development of teaming relationships through agreements with industrial partners is a key element of the Argonne (ANL) program.

Technical Highlights

Recent results are presented on $YBa_2Cu_3O_x$ (Y-123) coated conductors, including fabrication by pulsed laser deposition and sol-gel techniques, and characterization of yttria-stabilized zirconia (YSZ) layers deposited by ion-beam-assisted deposition (IBAD) and of MgO layers deposited by inclined substrate deposition (ISD); improved flux pinning at 77 K in Ag-sheathed $(Bi,Pb)_2Sr_2Ca_2Cu_3O_x$ (Bi-2223) tapes; and, in relation to fault-current limiters, effects of transient magnetic fields on a superconducting cylinder.

Fabrication of Coated Conductors by Pulsed Laser Deposition

Y-123 films were deposited by pulsed laser deposition (PLD). The excimer laser wavelength was 248 nm and the pulse width was 25 ns. Pulse energy of 160 mJ, pulse repeat rate of 8 Hz, and an oxygen pressure of 250 mtorr produced a growth rate of ≈0.25 nm/s. For deposition of the CeO_2 layer, 1 Hz and 300 mtorr of oxygen pressure were used. Substrates were mounted with Ag paste to a heated sample stage. Targets were rotated during deposition. The distance between the target and the substrates was 7.5 cm.

Three types of substrates were used for the deposition of Y-123 thin films:

(1) (001)-oriented $LaAlO_3$ (LAO) single crystals for initial optimization of the growth conditions;

(2) Hastelloy C (HC) substrates coated with biaxially textured YSZ buffer layers that were deposited by IBAD;

(3) Hastelloy C substrates with biaxially textured MgO buffer layers grown by ISD.

The structure of the films was examined by scanning electron microscopy (SEM) and X-ray diffraction (XRD), including pole figures and ϕ scans. T_c and J_c values for all films were measured inductively. For some of the films, transport J_c was also measured, with or without an applied magnetic field. For the transport measurements, an Ag film ≈2 μm thick was coated on the Y-123, and the composite films were annealed for 2 h in O_2 at 450–500°C.

(1) Y-123 films grown on (001) LAO substrates

Y-123 films were deposited on (001) LAO substrates at substrate temperature (T_s) values of 745, 755, 765, 770, 780, 790, 800, and 810°C to optimize deposition temperature, oxygen pressure, and annealing conditions (Table 1). The thickness of the films was ≈0.3 μm for a 22 min deposition. Several thicker films of 1 μm were deposited to achieve a higher I_c and J_e.

XRD confirmed the c-axis-oriented growth of the films. In the temperature range that we studied, a higher deposition temperature led to a higher T_c in the resulting Y-123 film. The best T_c and J_c values were obtained at T_s = 790°C: T_c = 90 K, transition width (ΔT) = 0.2 K, inductive J_c > 3.3 MA/cm^2, and transport J_c = 2.4 MA/cm^2. For example, Fig. 1 shows the transport J_c results of a Y-123/LAO film (Specimen 0530A, 1.0 μm thick, width = 5 mm) deposited at 790°C, with inductive J_c = 0.8 MA/cm^2.

Table 1. Superconductivity data for Y-123/LAO films

Samples	T_s (°C)	Thickness (μm)	T_c(K)	ΔT_c (K)	Inductive J_c (MA/cm^2)	Transport J_c (MA/cm^2)
0731A3	745	0.3	85.0	>2.0	1.0	-
0728A3	755	0.3	86.0	0.8	2.6	-
0714A1	765	0.3	86.2	0.9	3.0	0.3
0717A2	765	1.0	86.0	0.8	>1.0*	0.7
0421A1	770	0.3	86.4	0.8	1.8	-
0509A	780	0.3	87.1	0.6	-	-
0530A	790	1	86.0	0.2	-	0.8
0517A2	790	1	89.9	0.4	-	0.7
0720A1	790	0.3	88.0	0.5	>3.3*	to be done
0508A1	800	0.3	87.0	0.6	2.77	2.4
0727A2	810	0.3	90.5	1.5	2.3	to be done

*J_c value exceeded range of inductive system.

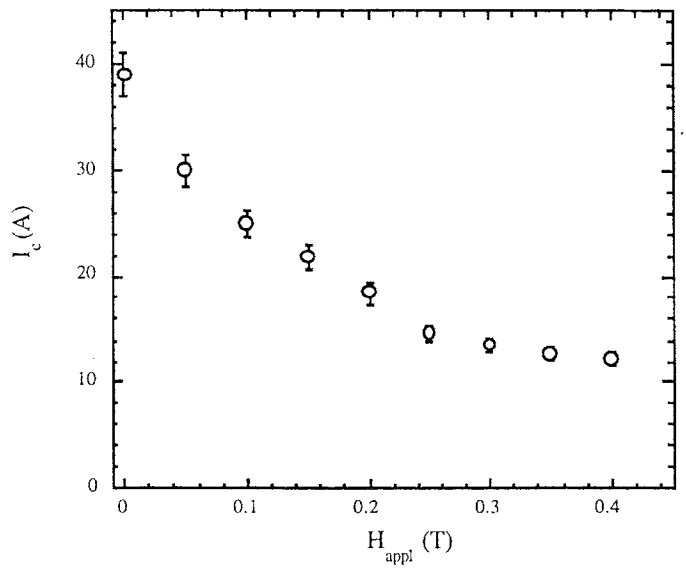

Fig. 1. Y-123/LAO films (0530A, 1.0 μm thick, width = 5 mm) deposited at 790°C. Inductive J_c = 0.8 MA/cm^2; also, J_c under applied magnet field.

Y-123 films with a thickness of 1 μm exhibited J_c values of 0.7–0.8 MA/cm^2, much lower than the 2.4 MA/ cm^2 obtained on a 0.3-μm-thick Y-123 film. Similar thickness dependencies have been reported by many others.

(2) Y-123 films grown on YSZ(IBAD)/HC substrates

Y-123 films were grown on YSZ(IBAD)/HC substrates at various temperatures (Table 2). The c-axis orientation and biaxial textures of Y-123 films were confirmed by pole figure analysis on these films (Fig. 2). The full width at half maximum (FWHM) values of the ϕ-scan peaks of the films are 15-18° and 18-22° for Y-123 and YSZ layer, respectively. Typical T_c values were 88 K, the transition width was ≈2 K, and J_c values were ≈0.2 MA/cm^2. Better texture will be required to obtain higher J_cs.

Table 2. Results of Y-123/YSZ/HC films

Samples	T_s (°C)	Thickness (μm)	T_c (K)	ΔT_c (K)	Inductive J_c (MA/cm^2)*	Transport J_c (10^5A/cm^2)
0526A	735	0.3	87.0	3.3	-	1.2
0525C	745	0.3	88.5	2.5	-	2.5
0524A	755	0.3	88.2	3.8	-	-----
0523A	765	0.3	86.8	~5.5	-	1.2

*There is no suitable conversion constant for Y-123/metal film to deduce the inductive J_c value.

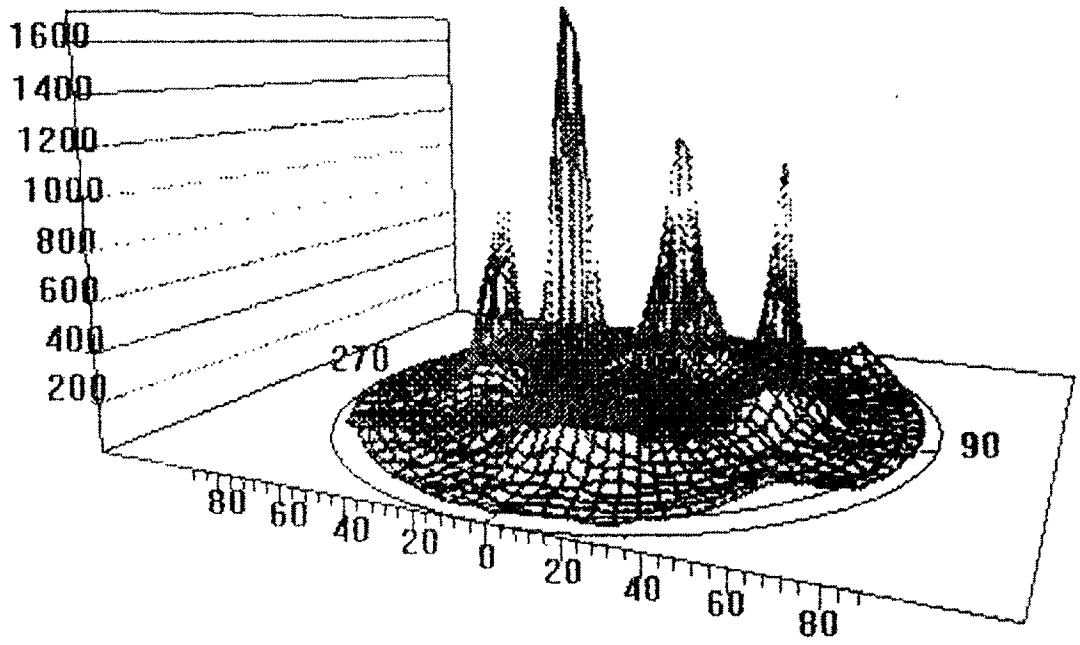
1600
1400
1200
1000
800
600
400
200
270
90
80
60
40
20
0
20
40
60
80

(a)

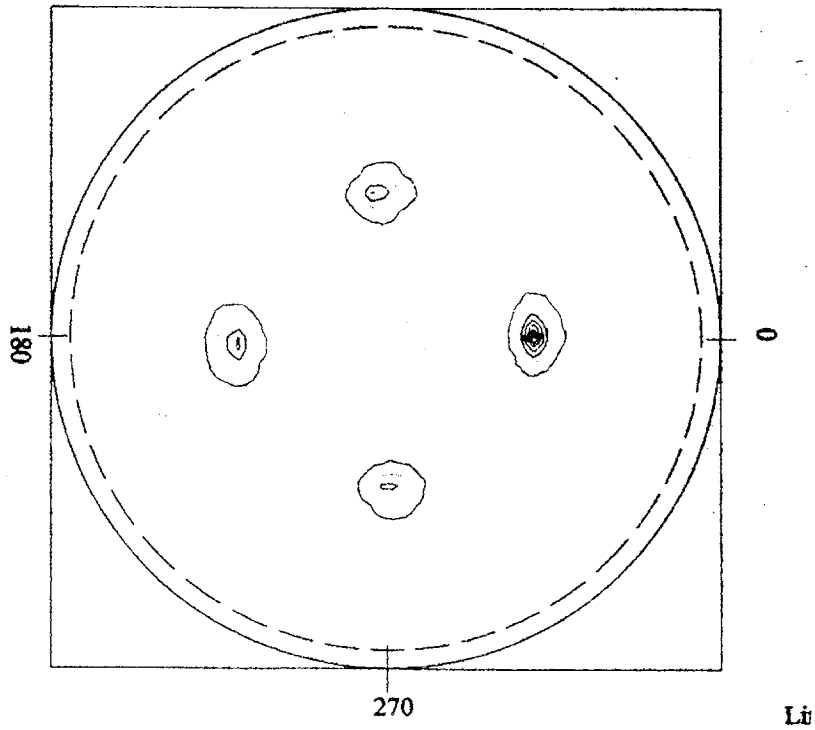
180
0
270
Li

(b)

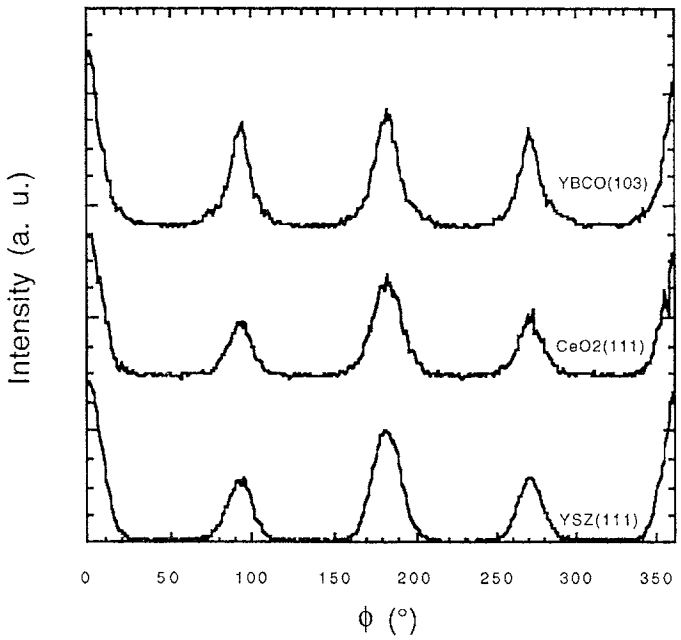

(c)

Fig. 2. Pole figures (a and b) and ϕ scans (c) of Y-123/CeO_2/YSZ/HC films (0607A2), FWHM ≈15-18° for Y-123(103) and 18-22° for YSZ(111).

To improve the lattice match between the Y-123 film and the YSZ buffer layer, a CeO_2 buffer layer was deposited on YSZ/HC by PLD (Table 3). Through use of these depositions, the Y-123 (100) orientation can be eliminated (Fig. 3) and T_c can be increased to ≈90 K.

(3) Y-123 films grown on MgO(ISD)/HC substrates

Y-123 films were deposited on MgO(ISD)/HC substrates. Buffer layers of CeO_2, $SrTiO_3$ (STO), or and MgO were deposited to improve the surface smoothness and the lattice match between Y-123 and the ISD MgO layer. The films that have been produced are shown in Table 4. Analyses are in progress.

X-ray pole-figure measurement of the Y-123/STO/MgO(PLD)/MgO(ISD)/HC reveals clear biaxial texture for both the Y-123 and the MgO (ISD) layers (Fig. 4). The tilt angles of the MgO layer and of the Y-123 film derived from the pattern is 30°.

Table 3. Results of Y-123/CeO_2/YSZ/HC films

Samples	T_s (°C)	Thickness (μm)	T_c (K)	ΔT_c (K)	Inductive J_c (MA/cm^2)*	Transport J_c ($10^5 A/cm^2$)
0609A2	750	0.3	90.0	5.0	-	1.2
0607A2	755	0.3	88.0	4.8	-	-
0612A2	755	0.3	90.0	5.0	-	1.0
0622A1	755	0.3	90.5	3.2	-	-
0621A	765	0.3	87.0	2.0	-	1.5
0627A	775	0.3	88.0	3.3	-	-

*There is no suitable conversion constant for Y-123/metal film to deduce the inductive J_c value.

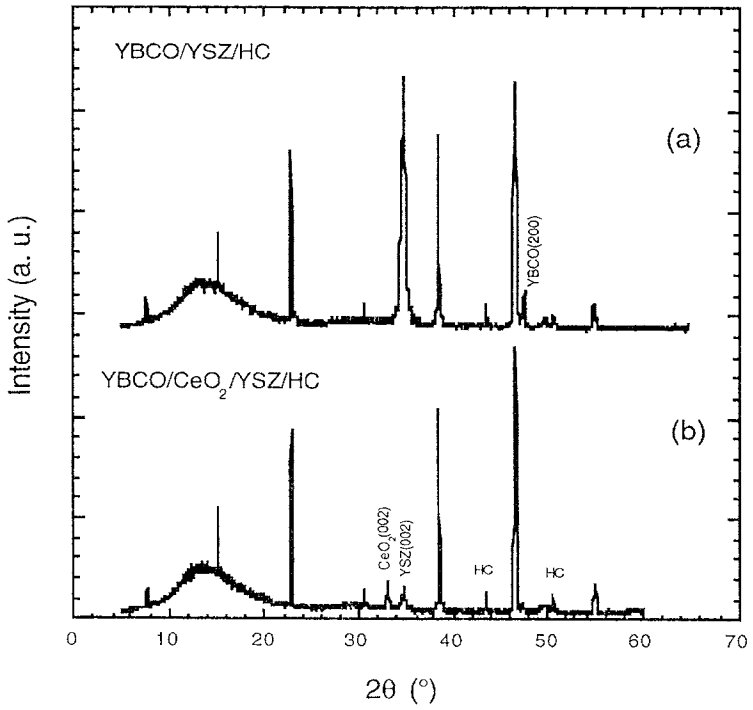

Fig. 3. 2θ diffraction pattern of Y-123/YSZ/HC and Y-123/CeO_2/YSZ/HC samples; Y-123 (100) peaks have been eliminated by the growth of CeO_2 buffer layer.

Table 4. Y-123 films grown on MgO(ISD)/HC substrates

Films	Description
Y-123/MgO(ISD)/HC	ISD MgO biaxially textured layer only
Y-123/CeO_2/MgO(ISD)/HC	Additional CeO_2 buffer layer introduced
Y-123/STO/MgO(ISD)/HC	Additional STO buffer layer introduced
Y-123/STO/MgO/MgO(ISD)/HC	Additional MgO and STO buffer layer introduced by PLD

To date T_c values have been <77 K, and so no J_c values have been measured. Clearly, either the MgO surface must be improved through cleaning and annealing and/or buffers will be needed between the MgO and the Y-123.

With respect to future work, the IBAD will focus on decreasing the FWHM. Successful ISD will require improvement in the matching of Y-123 to MgO. Annealing conditions must also be optimized for the Ag coatings on the Y-123 thin films for transport J_c measurements.

Deposition of IBAD Buffer Layers for Coated Conductors

Previous work has firmly established that the degree of texture development in YSZ films produced by IBAD is primarily dependent on the ratio of ions to atoms (r-value) arriving at the substrate surface during processing. The r-value can be changed by varying the ion beam current density (I_b) and deposition rate.

Based on work reported in the June 2000 Quarterly Report, we have constructed an IBAD YSZ texture/processing contour map (Fig. 5). Thickness and texture data were integrated to quantitatively map out the zones of preferred YSZ orientation. The two most easily changeable and important variables in the development of texture are the atomic and ion fluxes, better described as the deposition rate and the ion current density. The data needed to generate relatively smooth contour lines (iso-FWHMs and iso-thicknesses) were calculated by fitting the experimental data to curve fits. The data within zones that were not heavily studied were generated by extrapolating appropriate individual curve fits. Most of the experimental data were gathered at deposition rates between 0.64 and 3.2 Å/s and at ion current densities between 150 and 350 $\mu A/cm^2$, at which the tendency for biaxial texture development was the strongest.

The zones that showed (111) and (200) preferred growth are shaded. The (200) preferred growth is presented as dark gray; it spans a large region and is present for r-values greater than ≈1.67. The (111) zone of preferred growth is marked by lighter

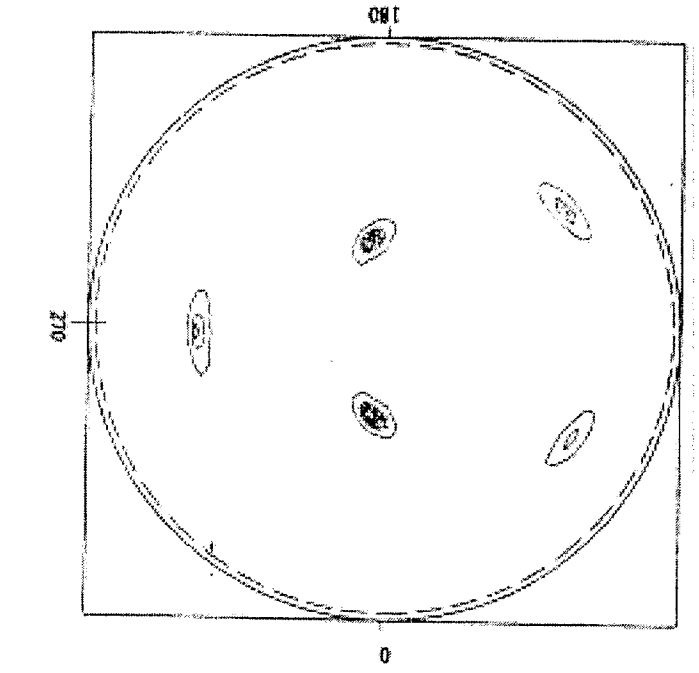

(a)

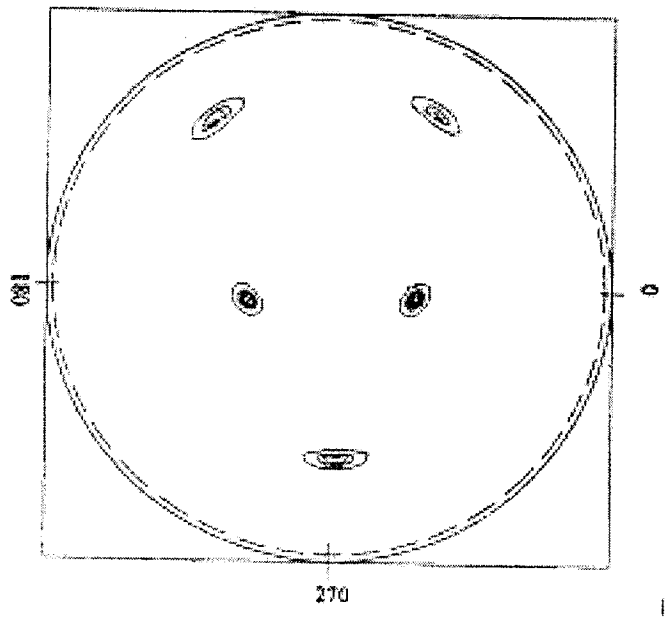

(b)

Fig. 4. Pole figure patterns of (a) MgO(220) plane and (b) Y-123(103) plane of Y-123/STO/MgO(PLD)/MgO(ISD)/HC sample.

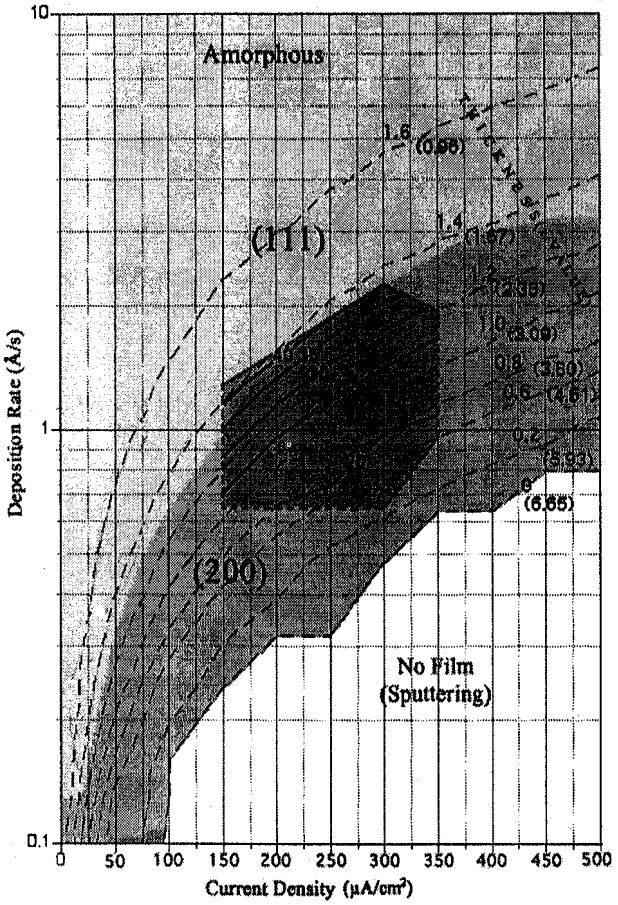

Fig. 5. Orientation of YSZ as a function of IBAD processing conditions.

gray and is found between the 1 and 1.67 r-value contour boundaries. There is little overlap of the (200) and (111) preferred growth that occurs at an r-value of ≈1.6. Thus, the small zone of (111) + (200) can be assumed to start at the (111) transition to the (200), proceeding to extend into and overlap a very small strip of the (111) zone. Low r-values, <1, produced YSZ films that were essentially amorphous. The boundary of transition from (111) to (200) preferred orientation approximately follows the 1.2 (1.67) thickness/r-value contour line. The (200) zone is present at $1.67 \leq r \leq r_c$, where $r_c \approx 6.65$, and marks the value at which sputtering overwhelms deposition.

The contour of zero thickness at the r_c marks the boundary at which the atom arrival rate and etching rate reach unity, and preferred (200) film growth begins. However, this boundary is not as well-defined as the line suggests. The processing zone between the zero and 0.2 thickness contour boundaries was highly susceptible to ion bombardment. Such large r-values introduced increased amounts of ion damage and stress between the film and substrate and was evident by visual inspection that revealed poor cohesion and delamination of the films deposited within this zone.

The region marked with heavy lines within the (200) zone represents biaxial texture development. Contained in this area are iso-FWHMs (lines of equal biaxial texture). FWHM data were obtained from films produced with ion current densities of 150–350 $\mu A/cm^2$. No FWHM data were obtained for very low deposition rates, which require excessively long processing times to reach the 1.6 μm thickness criterion. Thus, the dashed borders represent the cutoff of data analysis. However, the biaxial texture zone can be expected to extend past the dashed regions following the isolines, eventually being pinched off at an r-value of ≈3, which corresponds to both low and high deposition-rate and current-density coordinates. This zone can be expected to extend through the (200) zone, terminating at the r_c contour boundary.

Y-123 thin films prepared by a solution process

For fabrication of coated conductors on metallic substrate, various processing methods have been investigated to achieve high J_c values. Metal-organic decomposition (MOD) or sol-gel processes, which are performed in nonvacuum environments, offer great promise because they are cost-effective and easily scalable. Solution techniques are now being studied by many researchers, and good results have been obtained. An MOD process based on trifluoroacetate (TFA) has produced some of the highest J_c values of all the solution techniques. However, its application to metallic substrates has not been consistently successful, mostly because of a lack of full understanding of the processing conditions and their relationships to resulting structures and properties. We are now working on systematically optimizing the parameters of the TFA process. $LaAlO_3$ (LAO) single crystals are being used as the substrate. With the idea of the application to metallic substrates, we are in particular concentrating on lowering heat-treatment temperatures.

Solutions have been prepared in ambient atmosphere. Metal acetates of Y, Ba, and Cu were weighed to 1:2:3 ratio, dissolved in trifluoroacetic acid, and refluxed for 4 h. The resultant solution was then dried in air to evaporate the solvent and obtain a blue solid residue. The solid residue was then easily dissolved in methanol. We made the total cation concentration 1.5M; this methanol-based solution was used in our experiments.

The solution was coated on LAO single crystals by dip or spin coating. The precursor film was converted to an epitaxial Y-123 film through two steps of heat treatments. In the first step at low temperature, a uniform solid film containing substantial fluorine formed. An epitaxial Y-123 film developed and the fluorine was eliminated with heating in Ar at higher temperatures. Four maximum temperatures, ranging from 720 to 780°C, were studied. After the firing steps, the composition of each final Y-123 film was determined by atomic emission

spectroscopy. T_c was measured inductively. Microstructure and texture were evaluated by SEM, XRD, rocking curves, and ϕ scans.

Microstructures of representative samples are shown in Fig. 6. Many pores and small particles were observed, which is typical of films fabricated by a post-annealing process. The films prepared at 720°C (Fig. 6a) and 740°C (Fig. 6b) consisted of several layers of c-plane and acicular, a-axis-oriented grains. The main texture of all of the films was c-axis-perpendicular. As can be seen in Fig. 6c, the 760°C sample exhibited few a-axis grains, indicating that the texture is improved at this temperature. In the film prepared at 780°C (Fig. 6d), numerous large particles were observed rather than acicular grains, and the Y-123 layers below the particles appeared to be smoother than in other samples. The large particles were Cu-rich. This suggests that a CuO-rich liquid phase begins to form at ≈780°C, enhancing growth of c-axis-oriented grains.

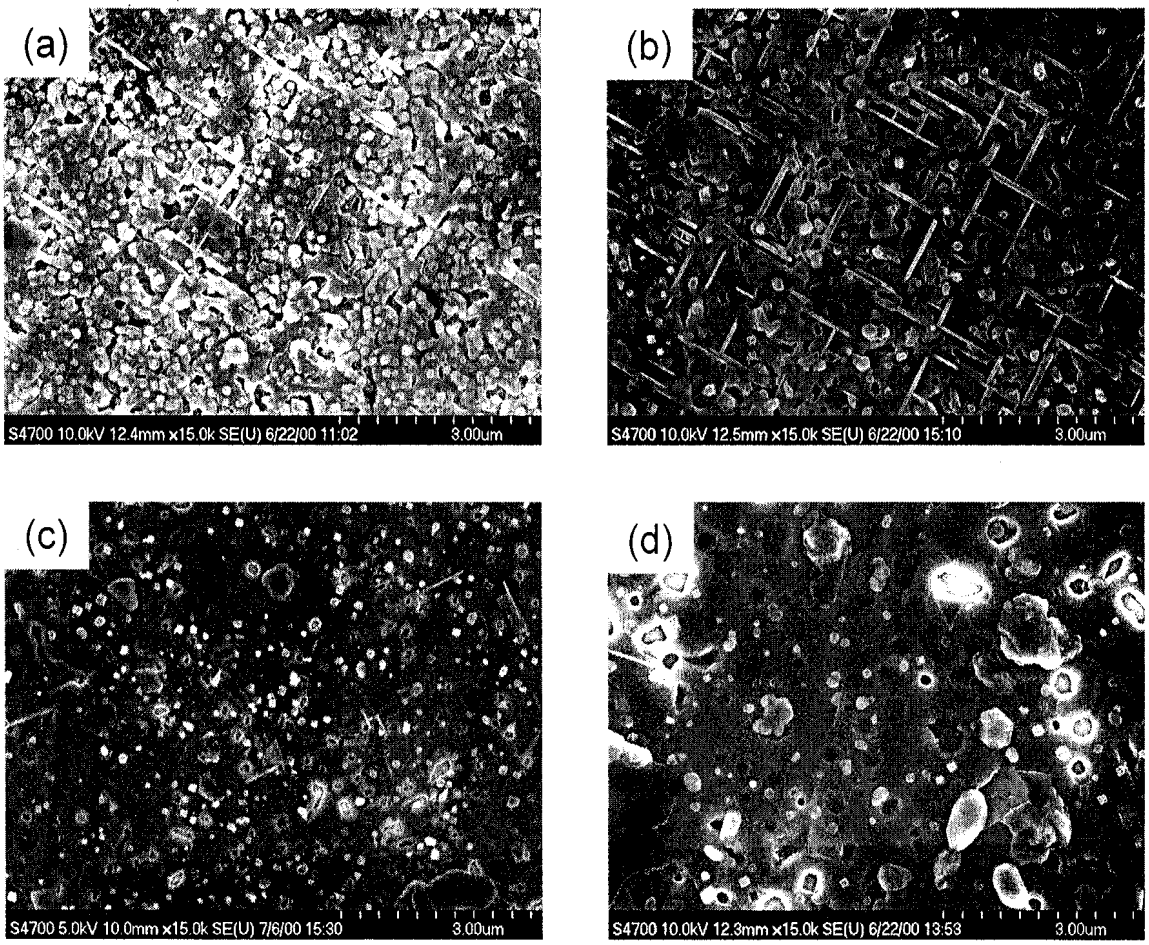

Fig. 6. SEM photomicrographs of samples prepared at (a) 720, (b) 740, (c) 760, and (d) 780°C.

Sharp T_c transitions were observed in films prepared at 740 and 760°C. For processing in Ar, temperatures between 740 and 760°C are thus considered to be optimal for forming the Y-123 phase.

Figure 7 shows (004) and (005) peaks of Y-123 films prepared at 720, 740, 760, and 780°C; the location of the strong (111) peak is marked by an arrow, but the peak itself is absent. The films were found to be highly textured, in spite of the frequently observed a-axis grains. However, impurity peaks, which are considered to come from second phases, were also observed in the XRD patterns.

In addition, the FWHMs of ϕ scans and rocking curves were measured to evaluate in-plane and out-of-plane textures. Figure 8 shows (113) ϕ scans of films prepared at 740 and 760°C. The FWHMs of the (113) peaks were <1° for both, indicating strong c-axis alignment of the grains. The FWHMs of rocking curves of the (002) peak were <0.5° (Fig. 9). These are excellent values in comparison to those found in the literature. In addition, the maximum heat-treatment temperature in our study was relatively low compared to the previously reported ones, which augers for succesful adaptation of this TFA process to coated conductors.

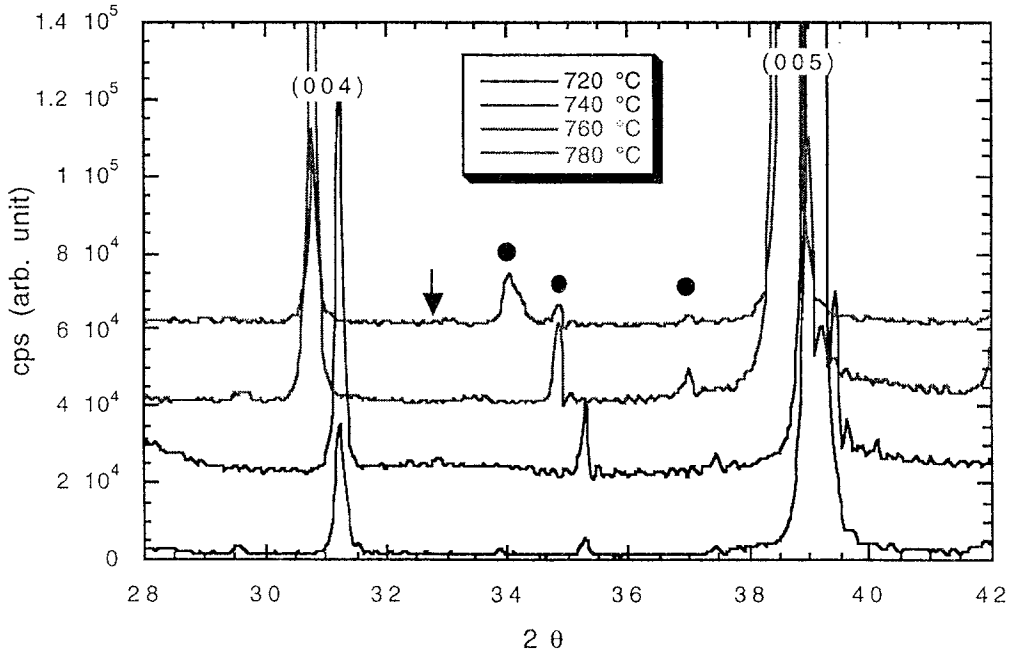

Fig. 7. XRD spectra that show strong texturing.

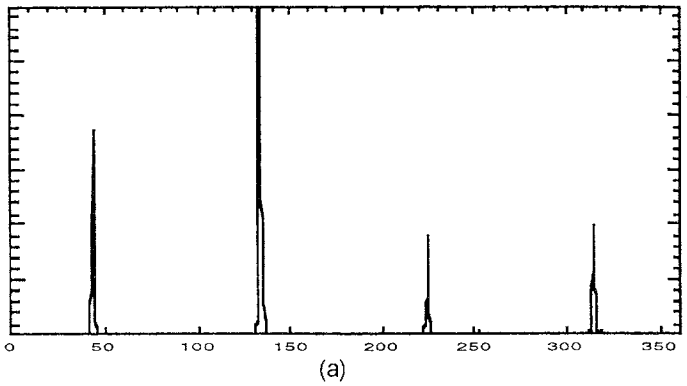

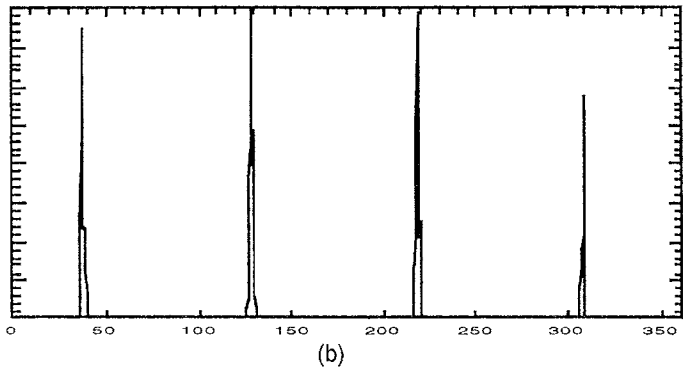

Fig. 8. ϕ scans of the (1 1 3) Y-123 peak of TFA-derived films produced at (a) 740 and (b) 760°C; FWHM values are <1°.

Characterization of Coated Conductors at the Advanced Photon Source

During FY 2000, we initiated studies aimed at developing and applying synchrotron-based X-ray diffraction, scattering, and spectroscopy methods to coated conductor substrates, buffer layers, precursors, and fully processed samples. This work is being done at the Advanced Photon Source (APS); it makes use of capabilities available at the Materials Research Collaborative Access Team (MRCAT) insertion device beamline located at Sector 10 (10-ID) of the APS. The X-ray beam at 10-ID is (1) high intensity (>10^{13} photons/sec), (2) highly collimated (≈0.002° beam divergence), and (3) tunable over a wide energy range (5 to 90 keV). The beamline is presently equipped with a well-instrumented X-ray spectroscopy bench and an 8-circle Huber goniometer that provides better than 0.02° resolution of diffraction lines in the $\theta/2\theta$ mode. Examples of some of the capabilities we are attempting to exploit for the detailed characterization of coated conductor embodiments during various stages of fabrication/processing are given below.

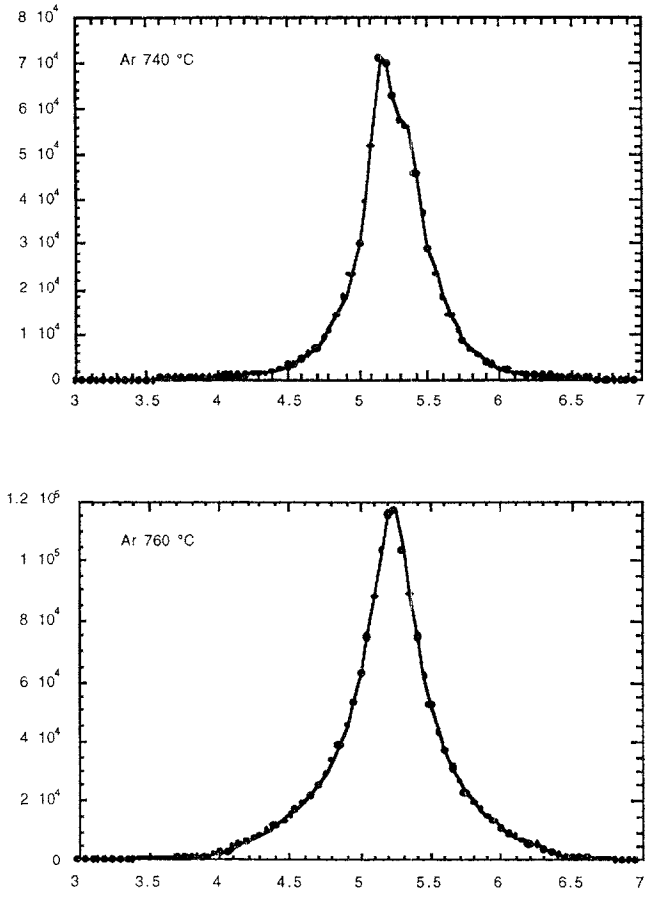

Fig. 9. Rocking curves of (0 0 2) peak of films produced at (a) 740 and (b) 760°C; FWHM values are <0.5°C.

The XRD pattern in Fig. 10 was obtained from a Y-123/CeO_2/YSZ/Inconel coated conductor sample on a coated substrate embodiment produced by the IBAD method, with the Y-123 applied by PLD. The pattern, recorded in 15 min with an unattenuated 11 keV beam (λ = 1.1271 Å), covers the 2θ range of the first ten [0,0,*l*] diffraction lines of Y-123 (many of which have saturated the detector), as well as specific diffraction lines for the underlying CeO_2 and YSZ buffer layers and the Inconel substrate. Detecting the strongest of the [0,0,*l*] reflections of well-textured Y-123 is normally not difficult with a modern laboratory X-ray source, but detection of the underlying buffer and substrate diffraction lines becomes more difficult as the Y-123 layer becomes thicker. The appearance in Fig. 10 of non-[*h*,0,0] diffraction lines for the substrate and buffer layers (albeit only weakly in some cases) has implications for the texture of the templating architecture underlying the Y-123 layer. Raman microspectroscopic examination of this sample revealed no evidence of second phases and none were detected in the XRD pattern of Fig. 10.

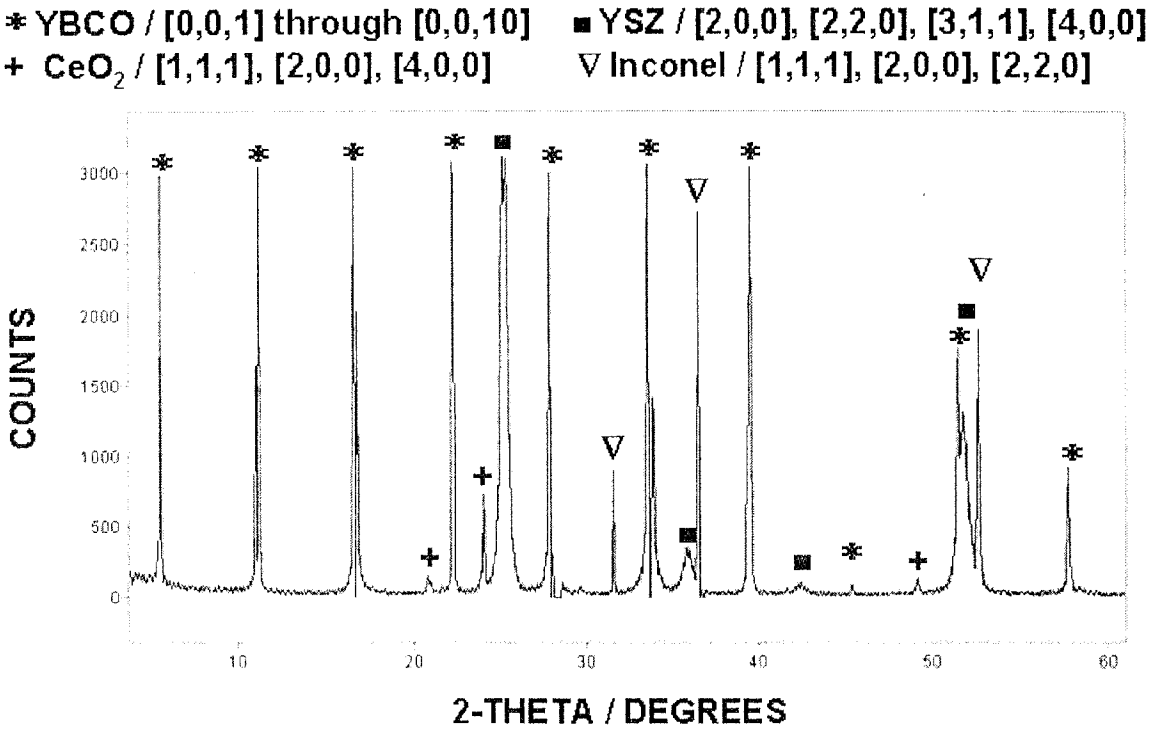

Fig. 10. Synchrotron θ-2θ XRD pattern of a Y-123/CeO_2/YSZ/Inconel coated conductor sample produced via an IBAD-processed substrate and PLD-deposited Y-123.

The patterns in Fig. 11 were obtained from Y-123 films supported on $LaAlO_3$ single-crystal substrates, with the Y-123 layers formed by heat treatment of dip-coated trifluoroacetate (TFA) precursors. From a correlation with Fig. 10, it is clear that most of the diffraction lines for patterns YJ21 and YJ38 in Fig. 11 are due to [0,0,*l*] lines of c-axis textured Y-123. However, the pattern for film YJ21 shows evidence of the presence of additional phases, as indicated in the scale-expanded segments of the pattern shown in Fig. 12. For the X-ray wavelength used in this measurement (1.1271 Å), most of the types of second phases one might expect to encounter for a TFA-based Y-123 film have the strongest diffraction lines in the 2-θ range from 15° to 35°. (This would include phases such as Y_2O_3, BaF_2, $BaCuO_2$, Y_2BaCuO_5, CuO, and non-[0,0,*l*] lines of Y-123.) The expanded pattern in Fig. 12 shows evidence of the three strongest lines of cubic BaF_2 (marked with black dots in Fig. 12), as well as the [1,0,3]/[1,1,0] line of Y-123 (black x) and a line indicated with a * that is believed to be the [2,0,0] reflection of Y-123, although it does occur near the expected 2θ value for [2,2,0] of $LaAlO_3$.

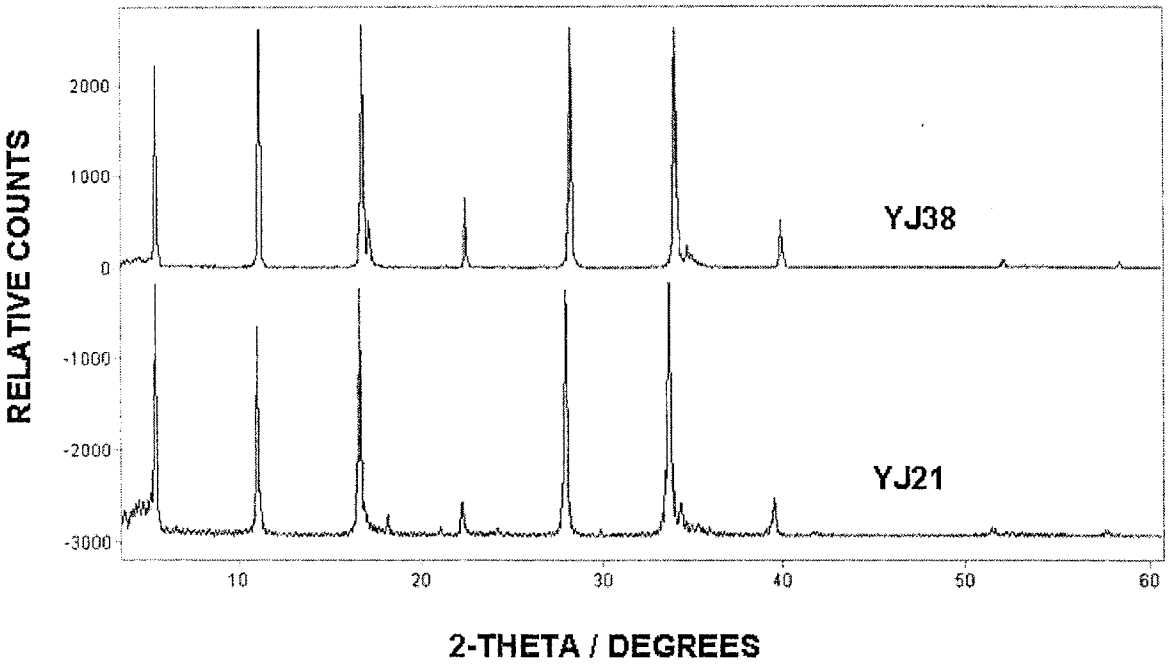

Fig. 11. Synchrotron XRD patterns of two Y-123 films deposited on single-crystal $LaAlO_3$ by the TFA dip-coat method. The five most intense lines (all [0,0,*l*]s of Y-123) are saturating the detector.

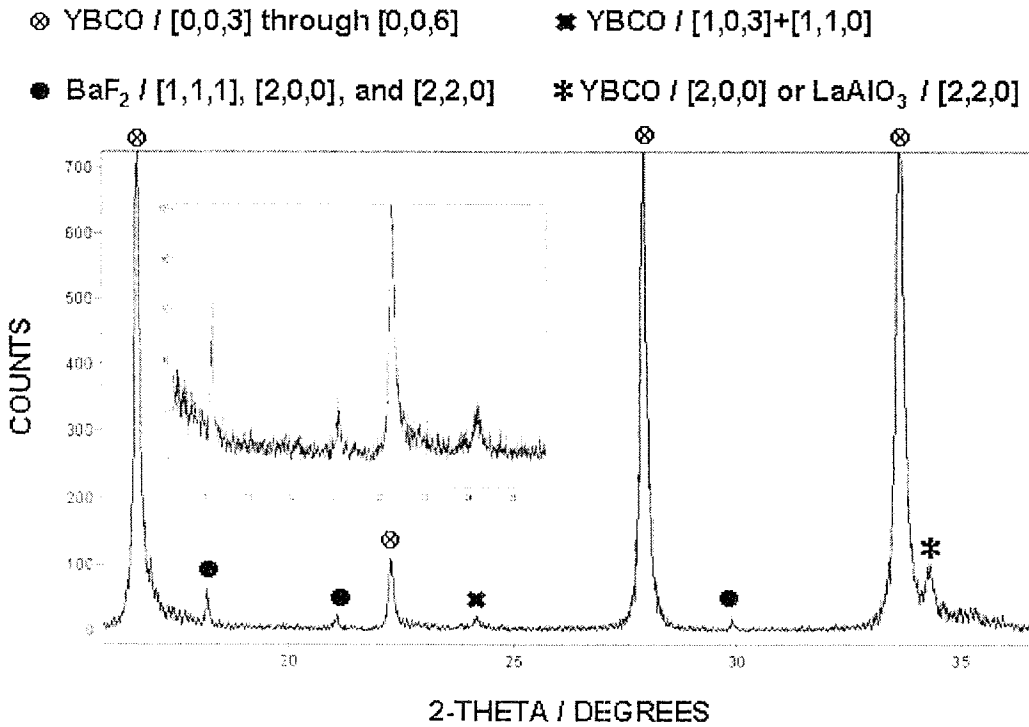

Fig. 12. Expanded view of the XRD pattern for sample YJ21 in **Fig. 2** showing evidence of BaF_2, and non-[0,0,*l*] lines of Y-123.

Figure 13 shows the rocking curve for the [2,0,0] diffraction line of a single-crystal YSZ substrate obtained directly from a TFA-type Y-123/CeO_2/YSZ coated conductor specimen. The insert displays the corresponding θ-2θ XRD pattern in the 24° to 26° 2θ range. In this range, one normally finds the [2,0,0] diffraction lines of YSZ and CeO_2 at 25.30° (d = 2.574 Å) and 24.04° (d = 2.706 Å), respectively, for λ = 1.1271 Å. It appears in the insert that the [2,0,0] of the CeO_2 layer(s) may be manifested at two somewhat higher 2θ values, indicating a more compressed structure. Specifically, we observe a weak diffraction line at 24.48° and a more intense one at 25.27°, which equate to d-spacings of ≈2.64 Å and ≈2.58 Å, respectively, assuming these two diffraction lines do emanate from the CeO_2 buffer layer structure. This interpretation of the diffraction pattern suggests that the CeO_2 film may be stratified into two or more layers with different [2,0,0] d-spacings. The sharp/narrow feature in the rocking curve is interpreted to be from the [2,0,0] reflection of YSZ indicated in the θ-2θ inset, where it appears at 25.34°, which gives a d-spacing of 2.570 Å for the YSZ single-crystal substrate (i.e., close to the accepted value of 2.574 Å). The broad underlying feature in the rocking curve is believed to be due to the [2,0,0] line of the ≈30-nm-thick compressed CeO_2 buffer layer. It is noteworthy that the diffraction pattern and rocking curve were obtained through a ≈0.5-μm-thick Y-123 over layer. We are continuing to investigate the utility of synchrotron-based X-ray diffraction methods for the quantitative in-situ study of stress/strain and misorientation effects in coated-conductor buffer layers.

Characterization of Coated-Conductor Specimens by Raman Microscopy

We continue to use Raman microscopy techniques to characterize coated conductors, substrates, precursors, and fully processed samples. The full-symmetry forms of orthorhombic (x=0) and tetragonal (x=1) Y-123 have distinct Raman spectra that contain (for each form) five readily detectable phonons. However, it is well known that Y-123 can also exist in several other types of stable and metastable structures and that these structures can coexist (see, for example, M. N. Iliev, Am. Chem. Soc. Symp. Ser. 730 (1999) 107). The Raman spectra of the various forms (and mixtures of forms) of Y-123 are sensitive to the types of structural perturbations that one must be concerned about during the preparation/fabrication of Y-123-based coated conductor materials. These can include (1) poor c-axis texturing, (2) cation disorder, (3) disconnected/fragmented metal-oxygen bonds (e.g., due to blotchy/incontiguous deposition), and (4) incomplete oxygenation. The frequency ranges of the five characteristic Raman phonons of orthorhombic and tetragonal Y-123 are summarized in Table 5, together with characteristic frequencies of other frequently observed coexisting phases.

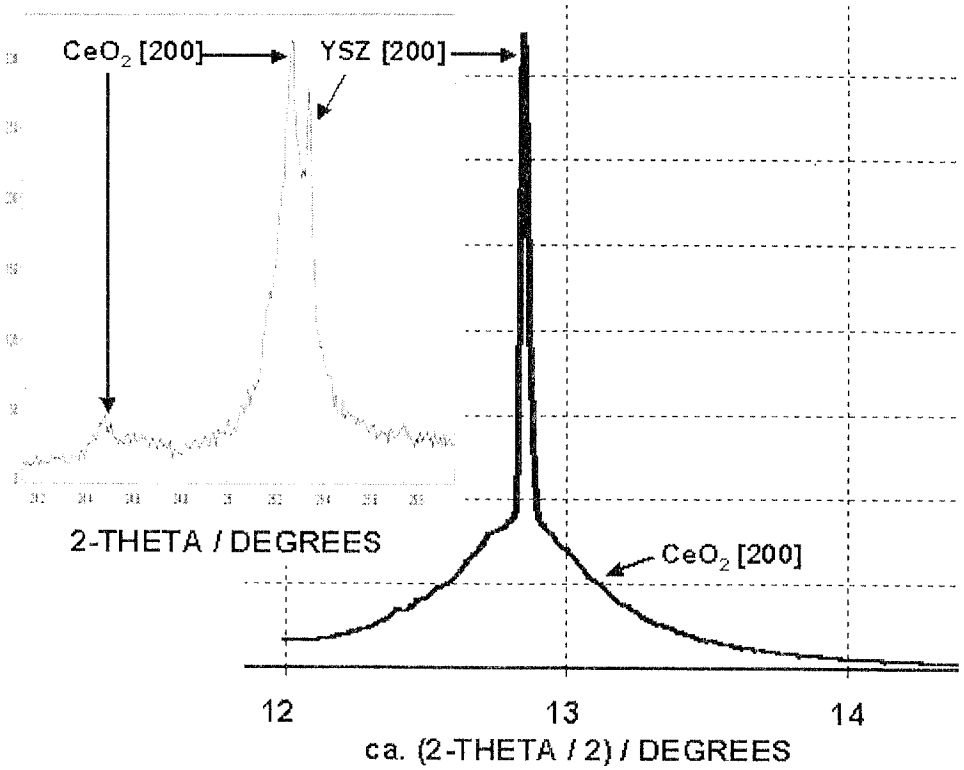

Fig. 13. Rocking curve for the [2,0,0] diffraction line of the YSZ (single-crystal) substrate in a Y-123/CeO_2/YSZ-coated-conductor embodiment, showing evidence of what appears to be a compressed CeO_2 buffer layer. Inset displays the local θ-2θ diffraction pattern.

Note especially in Table 5 the two modes for disordered types of Y-123 structures (Y-123-D) typically observed at ≈225 cm^{-1} and ≈585 cm^{-1}. The 225 cm^{-1} mode is reported to be associated with domains of broken metal-oxygen (M-O) chain structures, such as in samples exhibiting clumpy/island-like deposits. It is known that the 585 cm^{-1} mode is clearly correlated with cation disorder in the Y-123 lattice (see, for example, G. Gibson et al., Physica C 333 (2000) 139). Also, it is important to note that each of the five characteristic phonons of $YBa_2Cu_3O_6$ and $YBa_2Cu_3O_7$ is sensitive to the angle of incidence of the Raman excitation laser with respect to the Y-123 crystallographic axes and the excitation/detection polarization orientations. In Raman microscopy examinations, the direction of the incoming laser radiation and the direction of the detected Raman scattering are typically the same, and that direction is usually perpendicular to the substrate surface, hence it is also perpendicular to the a-b planes of the Y-123 film (for well-textured samples). Under these excitation/detection conditions (referred to hereinafter as the *xx/yy* orientation), the 340/335 and 140/150 cm^{-1} modes of $YBa_2Cu_3O_6$ and $YBa_2Cu_3O_7$ are considerably more intense than the other three modes. In particular, for perfectly textured Y-123, the 475/505 cm^{-1} mode should be weakest of all. The appearance of

Table 5. Characteristic Raman frequencies of Y-123 and common coexisting phases

Phase	Characteristic Phonon Mode Frequencies (cm^{-1})‡
$YBa_2Cu_3O_6$	115 140 340 450 475
$YBa_2Cu_3O_7$	115 150 335 435 505
Y-123-D*	225 585
$BaCuO_2$	585(m)
CuO	635(s)
Y_2BaCuO_5	290(s) 630(m)
	390(m) 605(s)

‡(m) and (s) indicate moderate relative intensity and strong relative intensity, respectively.
*Y-123-D indicates normally inactive Y-123 phonons that become active through loss of inversion symmetry or disorder.

this telltale Y-123 mode in *xx/yy* orientation is generally indicative of the presence of poorly textured domains, wherein Y-123 grains are puckered or tilted upwards with respect to the substrate surface. In addition, since the frequency of this mode for $YBa_2Cu_3O_{7-x}$ varies monotonically from x=1 to x=0, it can be used as an approximate indicator of the oxygen stoichiometry of the Y-123 phase.

Recent Raman microscopy examinations of Y-123 coated conductor specimens on single-crystal and textured metal substrates have produced spectra that are highly useful in gauging the quality of the Y-123 deposit. These specimens have come from IBAD, ISD, and TFA deposition processes. The spectrum in Fig. 14 was obtained from a TFA-based film deposited on an $LaAlO_3$ single crystal and processed at 780°C. In this spectrum, the laser has been defocused over a ≈30-μm-diameter domain. An interpretation of the spectral features is given in Fig. 14. Note that there is evidence of $BaCuO_2$, possible cation disorder (although this is difficult to determine with certainty in the presence of $BaCuO_2$ because of overlapping phonons), a less than optimally textured $YBa_2Cu_3O_{7-x}$ phase with $x \rightarrow 1.0$ (as indicated by the intensity of the 475/505 cm^{-1} phonon and its appearance at a value of ≈500 cm^{-1}), and some degree of M-O chain disruption.

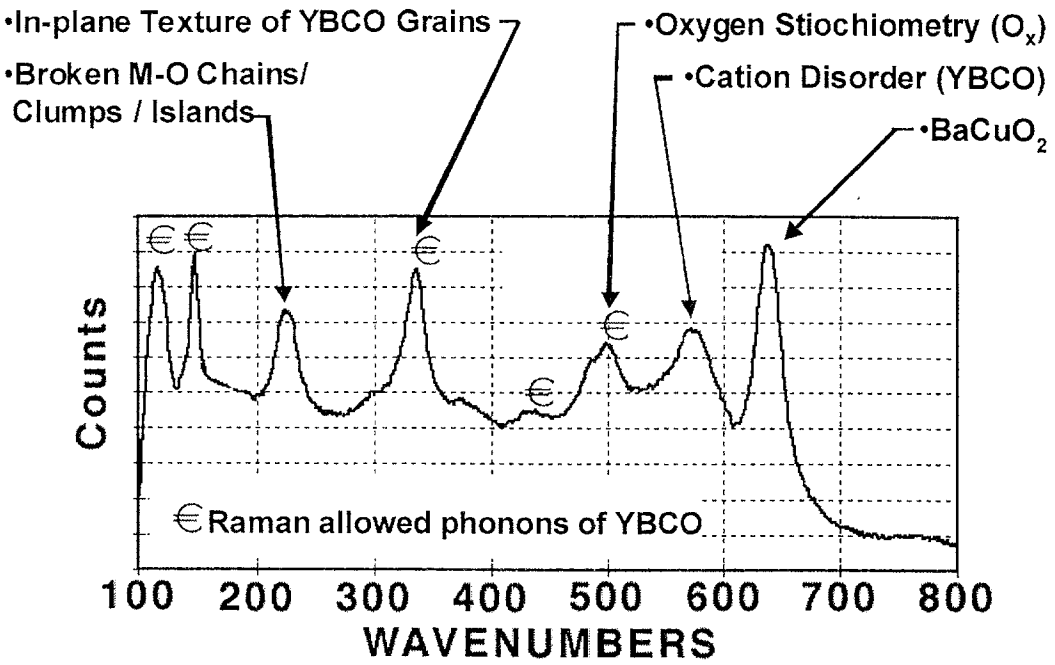

Fig. 14. Raman spectrum of a Y-123 film on an $LaAlO_3$ single crystal substrate, showing many of the features typically observed for Y-123-coated-conductor specimens.

TFA-type Y-123 precursors processed at progressively lower temperatures (<780°C) showed less and less $BaCuO_2$, but evidence of cation disorder (585 cm^{-1}) persisted. This is shown clearly in Fig. 15. It is also evident that the samples processed at the two lower temperatures (740 and 720°C) suffered less from the occurrence of broken M-O chain structure domains, but contained increasingly greater amounts of CuO (≈290 cm^{-1} mode).

Figure 16 shows Raman microscopy results for an IBAD sample and two ISD samples on textured Inconel substrates. The text blocks to the right of each spectrum in Fig. 16 outline the interpretation of the results. Comparison of the results in Figs. 15 and 16 reveals that the best samples in terms of Y-123 texture, phase purity, M-O disruption, and cation disorder are those produced by the IBAD process. These are also the coated-conductor samples that have exhibited the highest critical current density values in our laboratory.

Figure 17 contains Raman microscopy results for two TFA-type samples (on single-crystal YSZ) produced by a collaborating organization. In each case, we present spectra for three different locations on the same sample to show the spot-to-spot variability we have regularly encountered with IBAD-, ISD-, and TFA-processed coated-conductor specimens. Referring to the two samples as S1 and S2, respectively, spectra S1-A, S1-B, and S1-C, when viewed in progression, indicate

Raman microscopy spectra of TFA-type YBCO samples on $LaAlO_3$ for four heat treatment (HT) temperatures: Note

-broken M-O chain structures set in above 740°C (1),

-evidence of CuO at the lower HT temperatures (2),

-reduction in in-plane texture for HT temperatures above 760°C (3) vs (4),

-evidence for orthorhombic YBCO (4),

-$BaCuO_2$ begins to appear for HT temperatures above 740°C (5),

-cation disorder persists for all HT temperatures (6),

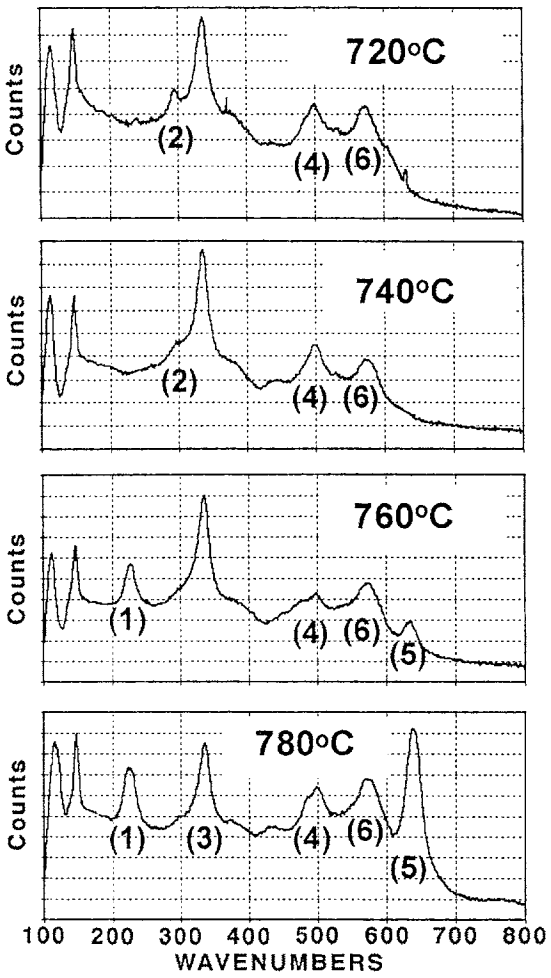

Fig. 15. Raman microscopy data for a series of TFA-based Y-123 films on $LaAlO_3$ single-crystal substrates. See descriptive text at left of each spectrum for a summary of the interpretation.

increasing amounts of M-O disruption (225 cm^{-1}), $BaCuO_2$ (≈630 cm^{-1}), and loss of Y-123 texture (the disappearance of the 335 cm^{-1} mode). The progression through spectra S2-A, S2-B, and S2-C reveals a similar result. In fact, there is almost no evidence of c-axis textured Y-123 grains in spectrum S2-C. Quite possibly, the $BaCuO_2$ impurity producing the strong scattering at ≈630 cm^{-1} could be deflecting the Y-123 grains around it out of the plane of the substrate. Raman images of $BaCuO_2$ crystallites embedded in Y-123 films on single-crystal and textured metal substrates show that these crystallites are mostly in the micrometer-size range and occur in patches, but some have in-plane dimensions of several micrometers - large enough to disrupt the Y-123 film texture during grain growth.

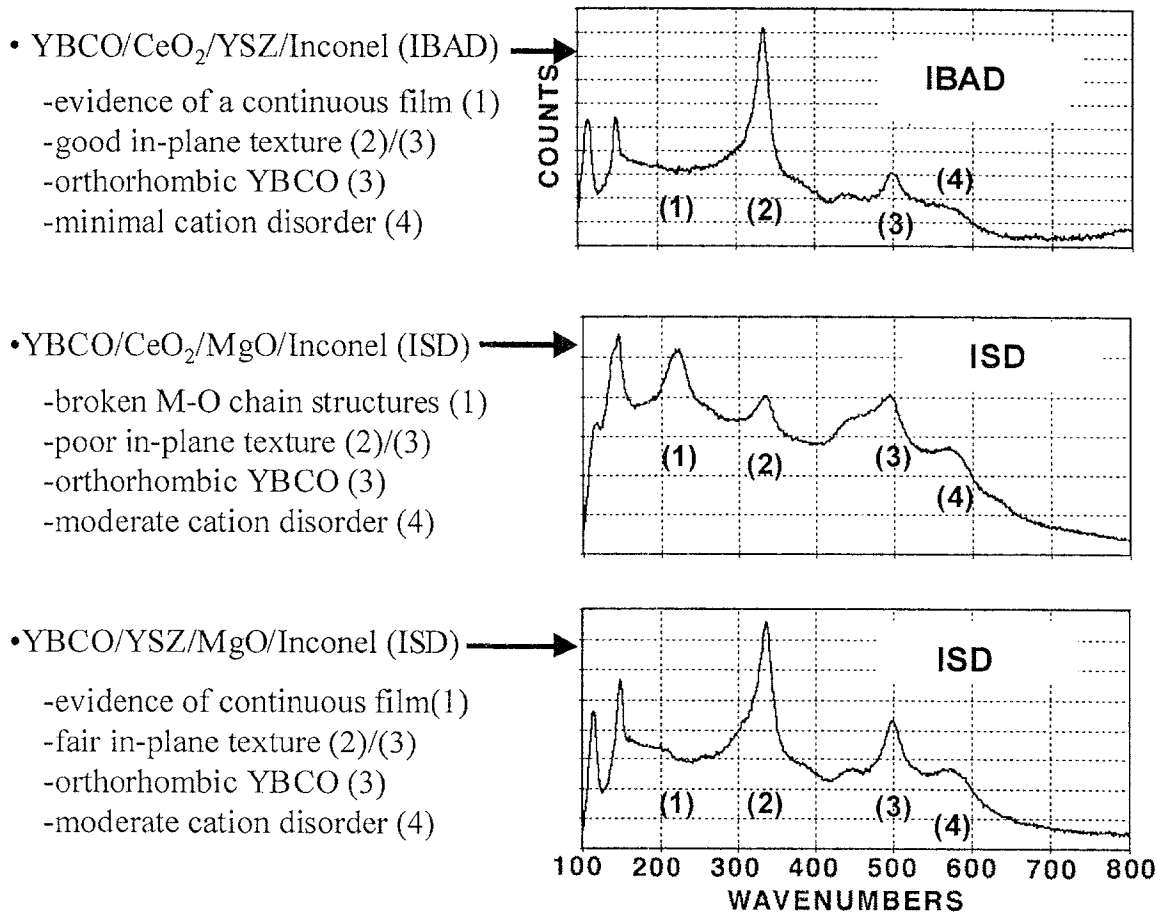

Fig. 16. Raman spectra of selected IBAD and ISD coated conductor samples. See descriptive text at left of each spectrum for a summary of the interpretation.

Bi-2223 Tapes with Improved In-Field Performance

First-generation $(Bi,Pb)_2Sr_2Ca_2Cu_3O_y$ (Bi-2223) superconducting tapes are used to build large prototype devices such as magnets, transformers, power cables, fault current limiters, and SMES units. State-of-the-art first-generation tapes are multifilament tapes made with Ag or Ag-alloy sheaths. They are typically 3.5 m m wide and 250 μm thick, >100 m long, and capable of withstanding 100 MPa tensile stress without degrading J_c values. They have a critical current $I_c \approx 50$ A at 77 K in self-field.

A goal is to improve pinning in Bi-2223 tapes. We have attempted to improve pinning by creating defects at the interface between Bi-2223 and MgO. This technique has yielded promising results that will be discussed.

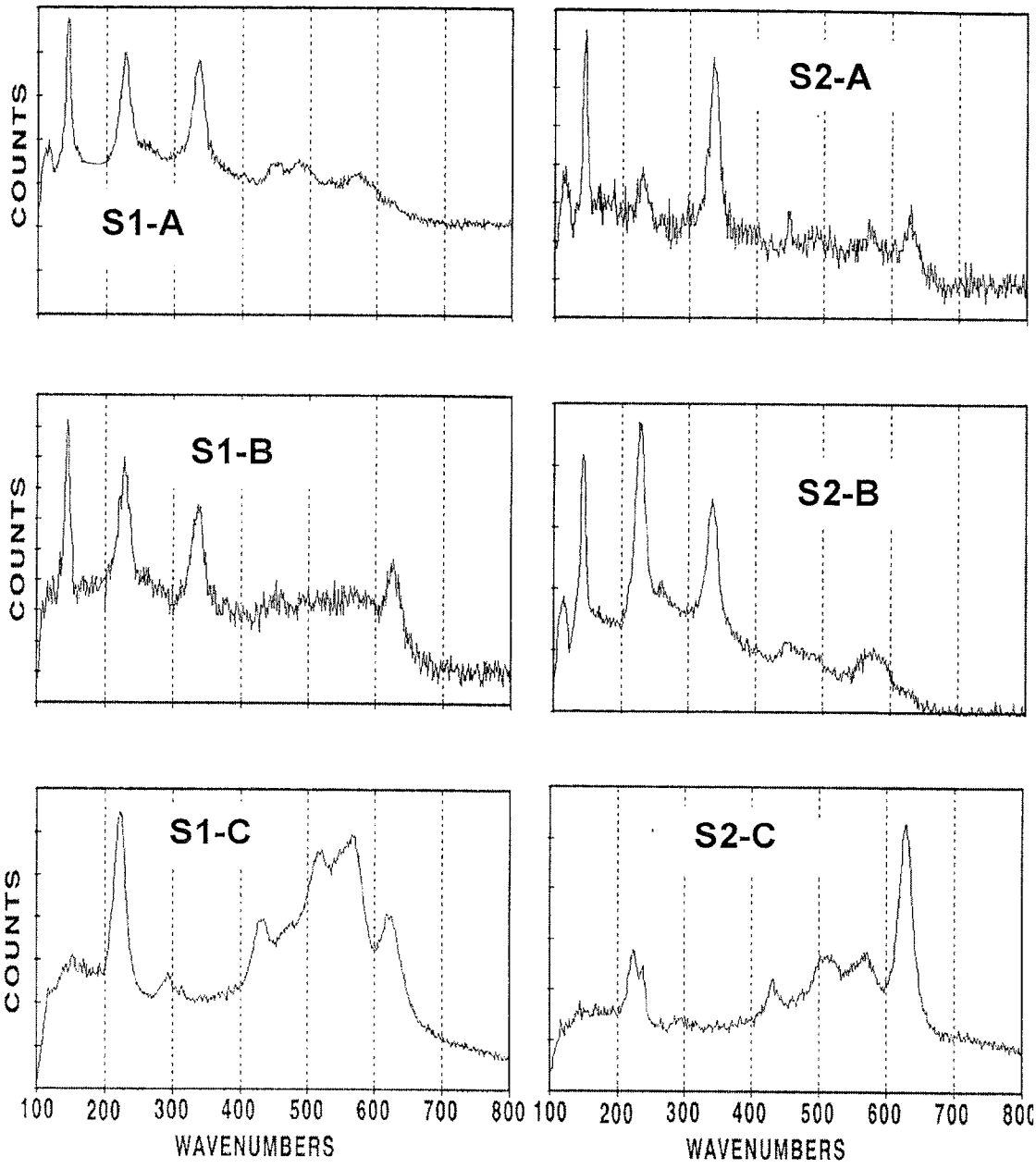

Fig. 17. Raman spectra of TFA-based Y-123 samples (S1 and S2) at different locations on the same sample, showing spot-to-spot variability.

The precursor powder was produced by the chemical precipitation method and contained Pb-added Bi-2212, Ca_2PbO_4, alkaline-earth cuprates, and CuO. Precursor powder particles were consolidated into billets by a drybag pressing method. The prepressed billets were inserted into Ag tubes, swaged, drawn through a series of dies, and then rolled to a final thickness of either ≈450 or ≈250 μm. Tape samples were cut and heat treated at 828°C in 8% O_2 atmosphere. The total annealing time was approximately 60 h. Each heat treating step was 30 h at the set point. A slow cooling schedule incorporated three cooling steps: 2°C/h for 8 h, 10°C/h for 10 h, and 60°C/h to RT. Cold pressing with 50-70 tons load was applied after the first heat treatment.

To make tapes with improved pinning, Ag was removed from one side of the as-rolled tape by chemical etching. The exposed side of the Bi-2223 was placed on an MgO single crystal and heat-treated, along with a reference tape under the same conditions. Following the first heat treatment, Bi-2223 adhered to the MgO single crystal. The composite Bi-2223/MgO tape was cold-pressed under the same load as the reference tape, and put through another heat treatment.

Bi-2223/MgO samples tapes were also fabricated on MgO films that were produced by electron-beam (e-beam) physical vapor deposition. The MgO was deposited to a thickness of ≈2.5 μm onto a Bi-2223 surface at a temperature of 750°C. Samples were then heat-treated under the same conditions as the Bi-2223 reference tape and the Bi-2223/MgO single crystal.

Microstructures were characterized by SEM and transmission electron microscopy (TEM), and chemical analysis was performed by energy-dispersive X-ray spectroscopy (EDS). Transport and inductive J_c values were obtained at 4.2 and 77 K.

TEM revealed that the contact between the Ag and Bi-2223 grains was excellent. XRD indicated that the c-axis of Bi-2223 was perpendicular to the interface.

Transport critical current was measured on short samples of Bi-2223/Ag tapes at 77 K. The following I_C measurements at 77 K in self-field were obtained after each heat treating step: 30-35 A after the first heat treatment, and 90-100 A after the second heat treatment. Figure 18 shows the I_C-H_{app} characteristics of the superconducting tape that carried 120 A in zero applied magnetic field at 77 K ($J_c \approx 3x10^4$ A/cm^2). Magnetic fields up to 0.4 T were applied perpendicular and parallel to the tape width. Magnetic field dependence at 77 K showed pronounced anisotropy for fields parallel and perpendicular to the tape width. A perpendicular field of 0.4 T lowers the I_c value from 120 to 5 A. A parallel field showed weak dependence: magnetic field of 0.4 T reduces the I_c value from 120 to 35 A.

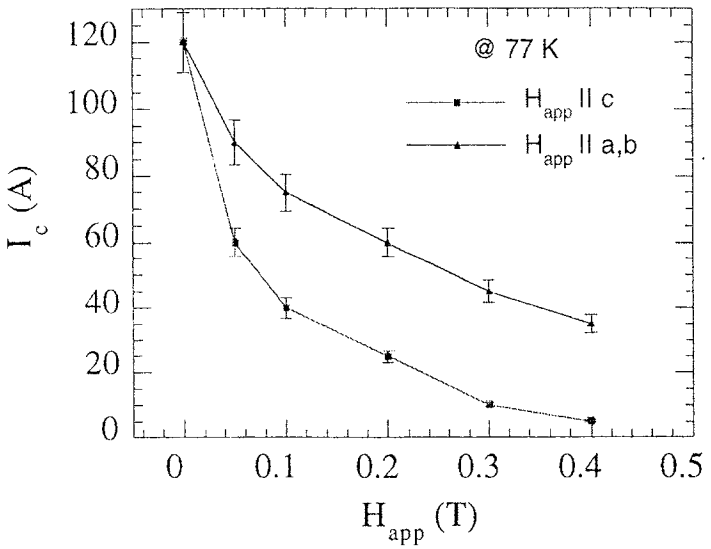

Fig. 18. Characteristic magnetic field dependence of transport critical current for multifilament Bi-2223/Ag tape at 77 K.

To characterize high-I_c tapes for high field applications at 4.2 K, a short sample (4 cm) that carried 120 A at 77 K was tested at 4.2 K in a field applied perpendicular to the width of the tape. An I_c value of 560 A was obtained in the self-field at 4.2 K ($J_c \approx 1.4 \times 10^5$ A/cm^2). After an initial drop to 310 A at 1 T, the critical current reaches a plateau and then declines to 245 A at 6 T. The observed I_c drop in the low-field region at 4.2 K indicates that connectivity and grain alignment of Bi-2223 grains could be further improved by a factor of ≈2.

A monofilament Bi-2223 reference sample was made by the technique stated above, heat-treated twice and pressed, and then measured for transport I_C at 77 K. Voltage vs. transport current characteristics for a thin Bi-2223 reference tape at 77 K with a magnetic field applied perpendicular to the width of the tape showed a sharp decrease. I_C decreased from ≈ 50 A at zero field ($J_c \approx 2 \times 10^4$ A/cm^2) to ≈ 2 A at 0.4 T. This clearly illustrates the weak performance of the Bi-2223 tapes at 77 K in applied magnetic field perpendicular to the width of the tape.

To improve pinning in Bi-2223 tapes, defects were introduced at the interface of the sample. Ag was removed from one side of the tape, and the exposed surface of the Bi-2223 was placed on an MgO single crystal. After the first heat treatment, good contact was developed along the interface between the Bi-2223 and the MgO single crystal. Transport critical current values for Bi-2223/MgO composite tapes were twice those for the Bi-2223 reference tape at 77 K in zero field. The tapes were cold-pressed and heat-treated again. High-magnification TEM was used to reveal at

higher resolution the nature of defects in Bi-2223 grains at the interface with MgO (Fig. 19). Defects that were perpendicular to the direction of current in Bi-2223 grains were observed.

After etching Ag, cold-pressing the Bi-2223 with the MgO, and during heat treatment, there is a chance of damaging the sample and causing the superconductivity to decrease. The thin Bi-2223/MgO sample showed a T_c of 109 K. It is apparent that the etching, pressing, and heat-treating has not decreased the T_c of the Bi-2223/MgO sample.

Figure 20 shows the normalized values for transport current in applied magnetic field for the thin Bi-2223 reference sample vs. Bi-2223/MgO sample. In a magnetic field of 0.4 T applied perpendicular to the width of the tape, transport critical current was about three times higher in the Bi-2223/MgO single crystal than in the Bi-2223 reference tape. I_c value in a field of 0.4 T decreased to ≈ 12% of the I_c value in the zero field for the Bi-2223/MgO sample, while the Bi-2223 reference sample decreased to ≈ 4%.

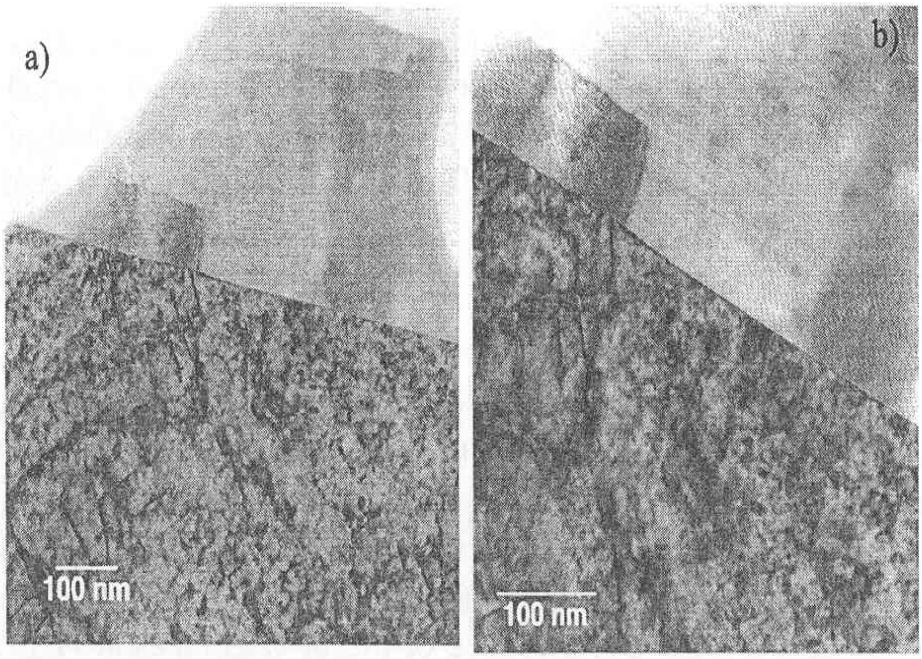

Fig. 19. High-magnification TEM photomicrographs showing interface between Bi-2223 and MgO single crystal after cold-pressing and second heat treatment: (a) ≈120,000x; (b) ≈200,000x.

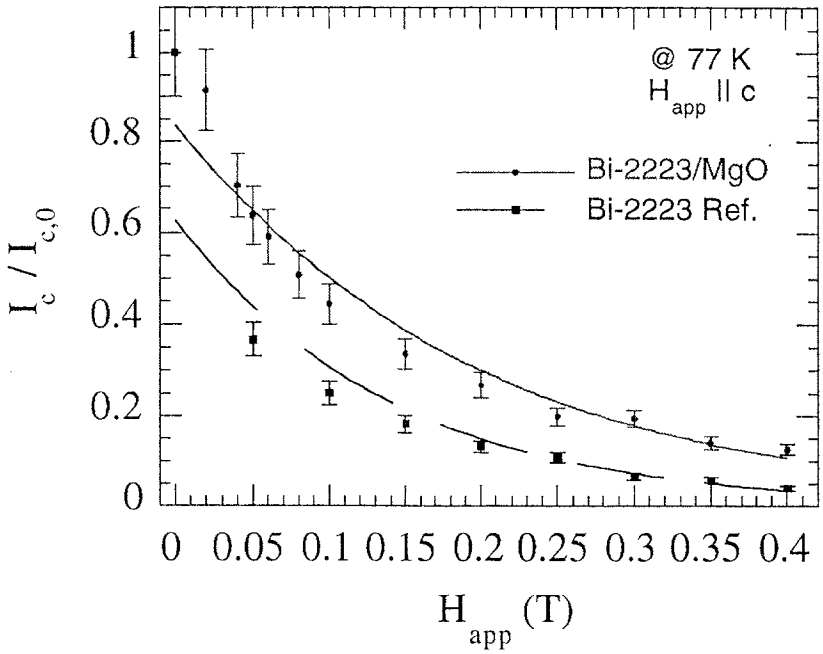

Fig. 20. Normalized transport current as function of applied magnetic field for thin Bi-2223 reference tape and Bi-2223/MgO tape at 77 K.

Samples of e-beam MgO were processed under the same conditions as the Bi-2223 reference tape and the Bi-2223/MgO single-crystal tape. (E-beam evaporation has potential industrial use; single crystals of MgO do not.) T_c was ≈102 K and inductive $I_{c,drive}$ was ≈150 mA for the Bi-2223/e-beam MgO sample ($J_c \approx 2 \times 10^4$ A/cm^2). However, the transport current measurements did not show improved pinning in these samples. The method is being examined further.

Transient Characteristics of Superconductor Tube Subjected to Magnetic Fields

Bulk high-temperature superconductors in the form of hollow cylinders or rings have two potential practical applications. The first is magnetic shielding and the second is in fault-current limiters (FCLs) for the power industry. A typical FCL consists mainly of an iron core inside a superconductor tube and a copper coil wound on the outside of the superconductor tube. When an FCL is used under normal operating conditions, the shielding capability of the superconductor tube keeps the impedance low. Under fault conditions, the large current in the copper coil exceeds the shielding capability of the superconductor tube and there is a jump in impedance because the iron core is no longer shielded from the coil by the superconductor tube.

In principle, the superconductor tube can provide shielding whether the source of the applied magnetic field is outside or inside the tube. We describe the results obtained at 77 K of induced current and transient characteristics of a melt- processed $Bi_2Sr_2CaCu_2O_X$ (Bi-2212) superconductor tube. Tests were conducted with copper coils placed either outside (externally applied field) or inside (internally applied field) the tube to study the differences in transient characteristics of these two configurations.

The pulsed current supply and the test setup are identical to those that we reported previously (Fig. 21). In the first test section, a copper coil is wound externally on the cylindrical superconductor tube. The coil has 80 turns, is ≈145 m m long, and has an inside diameter almost identical to the outside diameter of the superconductor tube. The Bi-2212 tube was 190 mm long, with a wall thickness of 8.0 mm and an outside diameter of 70 mm. A Hall probe was placed at the center of the tube to measure the axial magnetic flux density B. To measure the leakage field, a second Hall probe was placed on the outside of the copper coil, at the same elevation as the Hall probe inside the tube. A Rogowski coil was employed to measure the induced current in the superconductor tube. Response times of both the Hall probe and the Rogowski coil were much shorter than the transient time of the present experiments. The second test section is similar to the first, except that the copper coil is placed inside the superconductor tube.

Figure 22 shows the measured current and field at relatively low excitation current. In this figure, N is the number of turns of the driving coil; I (shunt) is the excitation current in the copper coil, measured by the shunt resistor; I (tube) is the induced current in the superconductor tube, derived from the signal of the Rogowski coil; B_i is the magnetic flux density, measured by the Hall probe inside the Bi-2212 tube; and B_O is the magnetic flux density, measured by the Hall probe on the outside of the superconductor tube.

Figure 22a shows that the field inside the tube (B_i) remains close to zero, which indicates that the externally applied field has not penetrated the tube. This finding is supported by the fact that the induced current I (tube) almost cancels the excitation current NI (shunt). A small field on the outside of the tube ($B_O \cong 10$ gauss) is the leakage field. This leakage field originates from one end of the external coil, circulates through a path outside the coil, and returns to the coil at the other end. Figure 22b shows that the applied field generated by the internal coil has also not penetrated the tube because the field outside the tube (B_o) remains close to zero throughout the test. The field inside the tube is much larger, with a maximum $B_I \cong 400$ gauss. The field inside the tube (B_i) represents the leakage field, which originates from the center of the coil and circulates around the internal coil,

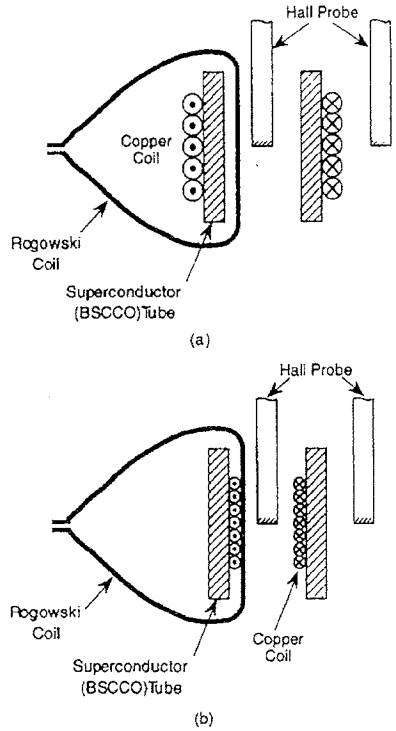

Fig. 21. Schematic diagrams of test section: (a) coil outside superconductor tube, and (b) coil inside superconductor tube.

through the gap between the superconductor tube and the internal coil. This leakage field is relatively high because all the fields are concentrated inside the coil, which has a limited volume. This is different from the case with the coil outside the tube, where the leakage field is circulating through an unbounded space. The current profiles in Fig. 22b are not as symmetric as those in Fig. 22a. Figure 22a shows that the profile of the induced current in the superconductor tube is almost a mirror image of the excitation current, indicating very good shielding and very little leakage field. This current symmetry with respect to the zero current axis is somewhat distorted in Fig. 22b. For example, the peak excitation current is ≈13,000 A, whereas the peak current in the superconductor tube is only ≈9,000 A. This difference in current is needed to support the relatively large leakage field, which is due to the 1-mm gap between the superconductor tube and the internal coil. Even though the leakage field is relatively large when the coil is inside, it is still capable of shielding the space outside the tube from the internally generated magnetic field at relatively low excitation current.

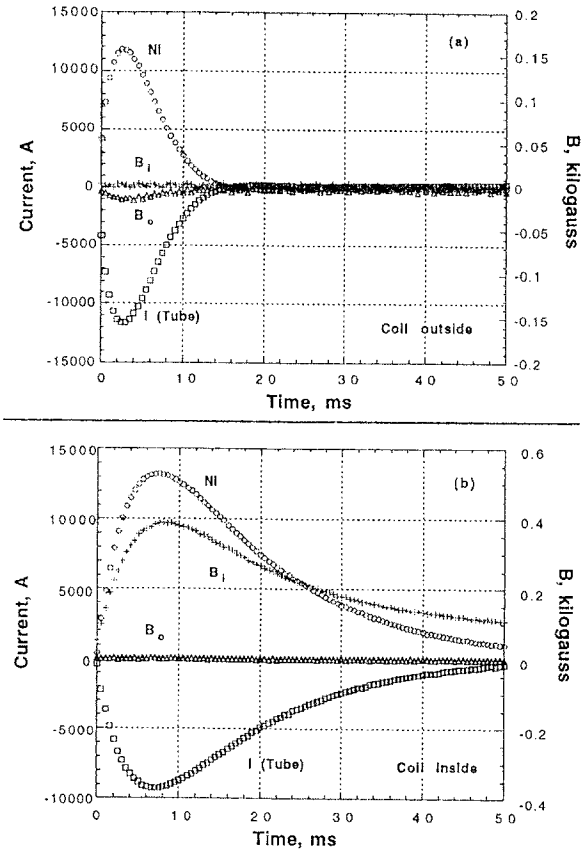

Fig. 22. Measured current and field at relatively low excitation current for (a) coil outside superconductor tube, and (b) coil inside superconductor tube.

Figures 23a and 23b show the measured current and field at some intermediate excitation current. The magnetic field inside the tube (B_i) (Fig. 3a) shows that 2 ms into the test, when the excitation current reached 32,000 A, the tube is just penetrated by the externally applied magnetic field. The interesting behavior is that when the excitation current NI begins to decrease, the magnetic field inside the tube continues to increase. This behavior can be explained by the concept of nonlinear magnetic diffusion. The results shown in Fig. 23b do not seem to indicate that the internally generated magnetic field has penetrated the tube because the field outside the tube (B_O) remains close to zero throughout the test. However, when the field outside the superconductor tube is plotted on a more sensitive scale, as shown in Fig. 23c, the data indicate that the internally generated magnetic field has penetrated the tube at t = 8 ms. This corresponds to a peak NI of ≈33,000 A, which equals the NI at penetration for the case of coil outside the tube.

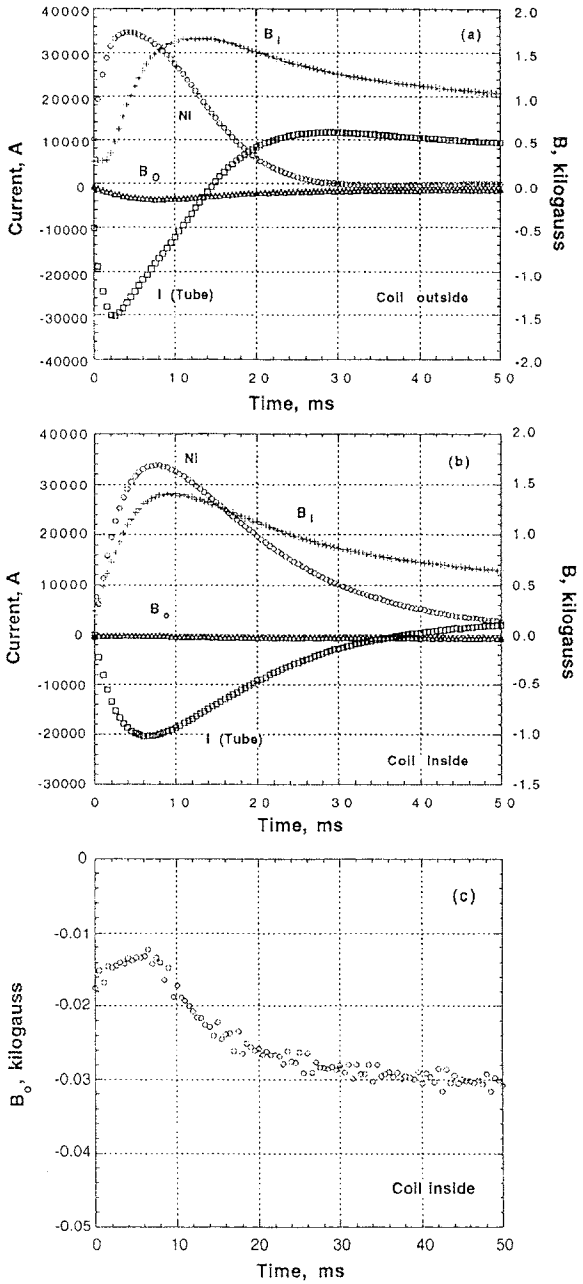

Fig. 23. Measured current and field at intermediate excitation current for (a) coil outside superconductor tube, (b) coil inside superconductor tube, and (c) coil inside superconductor tube, results plotted on more sensitive scale.

Figures 24a and 24b show the measured current and field at relatively high excitation current. With the coil outside the tube, the data for B_i clearly indicate that the externally applied field penetrated the tube in 1.5 ms, and this occurred at NI ≅ 40,000 A. Figure 24a shows that again there is a delay between the peak NI and the peak B_i. When the coil is inside the tube, the data for B_O in Fig. 24b indicate that the

internally generated magnetic field has penetrated the tube and affected the field outside the tube. The data indicate that field penetration occurred at t = 3.5 ms, which corresponds to NI = 52,000 A.

Several features are common to both test configurations. First, both tests show that there is a delay between the peak NI and peak penetration field (peak B_i for coil outside and peak B_o for coil inside). This delay decreases with increasing peak NI. For example, the delay between peak NI and peak B_i is 8 ms for peak NI = 34,000 A (Fig. 23a). This delay decreased to 3 ms when peak NI = 65,000 A (Fig. 24a). Similar behaviors were observed for the case with coil inside the superconductor tube. Second, both test configurations show that the value of NI and I(tube) at field penetration depends on the ramp rate of the excitation current (dI/dt). Third, both test configurations show that the time at field penetration determined by the Hall probe coincides approximately with the time when the induced current I(tube)

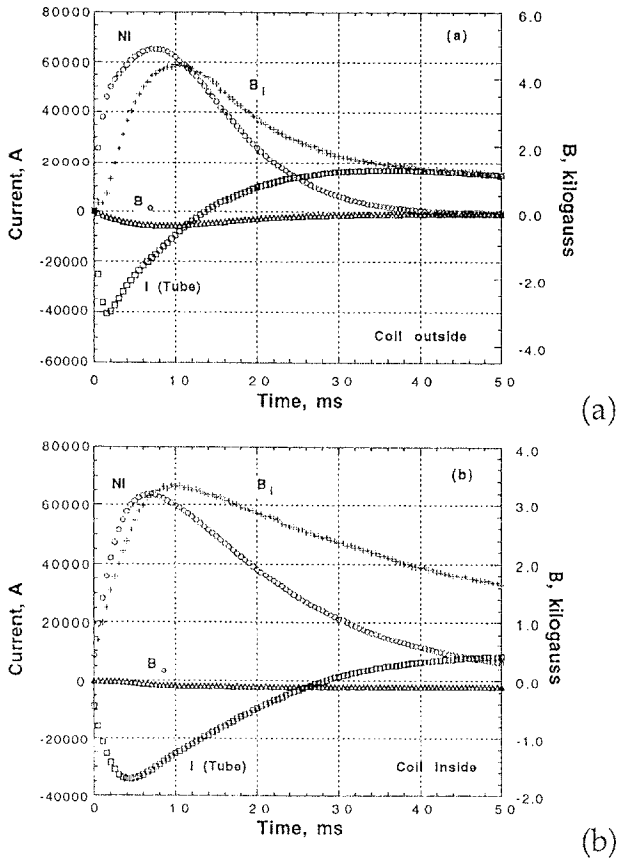

Fig. 24. Measured current and field at relatively high excitation current for (a) coil outside superconductor tube, and (b) coil inside superconductor tube.

reaches its maximum value. Finally, all of the tests show that the induced current was initially negative and opposite the direction of the excitation current, but eventually the induced current crossed over the horizontal axis and became positive to support the trapped field inside the superconductor tube.

High-T_c superconductors usually follow the so-called power law in the flux creep regime, and the resistivity is a function of current. It can be shown that the magnetic diffusion equation becomes nonlinear when the resistivity depends on the current. For cylindrical geometry, the one-dimensional, nonlinear magnetic diffusion equation takes the form

$$[\partial(D_m r \partial B_z/\partial r)/\partial r]/r = \partial B_z/\partial t\,, \tag{1}$$

where B_z is the magnetic flux density in the axial direction, r is the radial coordinate, t is time, and the magnetic diffusion coefficient D_m is given by

$$D_m = \rho(J) / \mu_o\,, \tag{2}$$

with the current-dependent resistivity $\rho(J)$ given by the power law. For melt-cast-processed Bi-2212 with a wall thickness of several millimeters, the characteristic diffusion time at 77 K and an electric field strength of 1 μV/cm is several hundred milliseconds. This is much larger than the rise time (several milliseconds) of the pulsed current in the present experiment. Therefore, magnetic diffusion is important and cannot be neglected. However, a characteristic diffusion time of several hundred milliseconds is too long for the Bi-2212 tube to be penetrated in the present experiment, which shows that penetration occurred in a few milliseconds.

Two factors increased the rate of magnetic diffusion and facilitated the field penetration of the tube. First, the speed of magnetic flux propagation (diffusion) strongly depends on the local resistivity ρ in the superconductor. During a transient, the local gradient of magnetic flux density can be greater than that of Bean's model, and the local current density can be greater than the critical current density at a field strength of 1 μV/cm. Local resistivity increases with current density, which speeds up the magnetic diffusion process because the magnetic diffusion coefficient D_m is linearly proportional to ρ. Second, when local ρ increases, so does dissipation (ρJ^2). If heat is not removed quickly enough from the superconductor, the local temperature will rise. When temperature rises, the resistivity increases, further increasing the magnetic diffusion coefficient, and speeding up the magnetic diffusion process. The observation that the penetrated field is still rising while the excitation current (NI) is decreasing is the result of magnetic diffusion. A finite time is necessary for magnetic flux density to diffuse from the interior to the boundary of the tube. When the excitation current begins to decrease, the flux density is greater inside the wall of the tube than outside the wall, magnetic diffusion is still in force and causes the penetrated field to increase. This

series of events cannot be explained by Bean's critical-state model, which is applicable to steady-state conditions only.

With regard to applications, such as fault current limiters (FCLs), the present experiments show that the leakage flux is greater when the coil is inside the tube than outside the tube. They also demonstrate that the superconductor tube is equally capable of shielding internally or externally generated magnetic fields. To further support this conclusion, we have measured the inductance ratio of these two configurations. The inductance of the outside coil alone was 0.22 mH; that of the outside coil with the superconductor inside (at 77 K) was 0.049 mH. The reduction in inductance was a factor of 4.48. The inductance of the inside coil alone was 0.096 mH; that of the inside coil with the superconductor outside (at 77 K) was 0.020 mH. Reduction in inductance was a factor of 4.80. Therefore, both configurations will work for an FCL and the reduction in inductance does not differ by much. However, under fault conditions, an FCL with a coil inside will have an inductance less than that of an FCL with a coil outside because, inherently, the latter has a larger volume than the former. Finally, it should be noted that the present experiments were conducted with an air core only and are different from the superconductor-shielded-core-reactor (SSCR), which usually contains an iron core. A closed iron-core SSCR is mostly a resistive device and is quite different from an air-core SSCR, which behaves more like an inductive device.

Interactions

From July though early September, Alicia Salazar, a graduate student from the University of Madrid, worked with J. P. Singh. Her goal was to fabricate high-quality bulk superconductors that are to be used in a series of studies of fundamental properties. Powders were synthesized and several bulk pieces were made.

On July 10, Balu Balachandran attended the ANL-IGC-LANL CRADA meeting at Los Alamos.

Balu Balachandran and Roger Poeppel attended the HTS Industrial Overview Committee (IOC) meeting at Los Alamos, August 28-29.

Balu Balachandran, Vic Maroni, John Hull, and Ken Gray participated at the HTS Annual Peer Review, Washington, DC, July 17-19.

Vic Maroni attended a Wire Development Group Meeting held in conjunction with the FY 2000 Peer Review in Washington, DC. The meeting date was July 20; the other attendees were from American Superconductor Corp., LANL, ORNL, and Univ. of Wisconsin–Madison.

A new Ph.D student from the University of Illinois at Chicago (UIC), Tim Weber, joined the superconductor program on September 11. He will be advised at UIC by Prof. M. J. McNallan. His project on substrate development in coated conductors will be supervised by Balu Balachandran.

Dr. M. B. Srinivas, School of Physics, University of Hyderbad, India, visited Argonne and on Sept. 15 gave a seminar on the dielectric needs for HTS applications.

Balu Balachandran, Beihai Ma, Brandon Fisher, John Hull, and Y. S. Cha attended the Applied Superconductivity Conference, Virginia Beach, VA, Sept. 18-21.

On Sept. 26, 2000, Dr. Gye Won Hong, Head, Functional Materials Group, Korean Atomic Energy Research Institute, Seoul, visited Argonne and gave a seminar on HTS activities in Korea.

List of Publications and Presentations

Published or presented:

Y. S. Cha, Magnetic Diffusion in High-T_c Superconductors, Physica C 330 (2000) 1-8.

K. C. Goretta, Mechanical Properties of Bulk High-Temperature Superconductors, Chapter in "Superconducting Materials: Advances in Technology and Applications," pp. 234-239, eds. A. Tampieri and G. Celotti (August 2000).

K. C. Goretta and N. Chen, Diffusion and Heat Treatment of High-Temperature Superconductors, Chapter in "Superconducting Materials: Advances in Technology and Applications," pp. 218-228, eds. A. Tampieri and G. Celotti (August 2000).

S. Salem-Sugui Jr. (Instituto de Fisica, Rio de Janiero, Brazil) and K. C. Goretta, Effect of Short-Time Magnetic Relaxation on Hysteresis Curves in Single-Crystal $Bi_2Sr_2CaCu_2O_x$, J. Supercond. 13 (2000) 367-370.

V. Selvamanickam, G. Galinski, G. Carota, J. DeFrank, C. Trautwein, P. Haldar (IGC); U. Balachandran, M. Chudzik; J. Y. Coulter, P. N. Arendt, S. R. Foltyn, B. Newnam, and D. E. Peterson (LANL), High-Current Y-Ba-Cu-O Conductor by Metal Organic Chemical Vapor Deposition on Metal Substrates, Physica C, Vol. 333 (2000) 155-162 .

B. I. Smirnov, T. S. Orlova (Ioffe Inst., Russia); S. Sengupta (Supercond. Comp., Columbus, OH); and K. C. Goretta, I-V Characteristics and the Electric-Field Effect in Melt-Grown $YBa_2Cu_3O_x/Y_2BaCuO_5$ HTSC Crystals, Phys. Solid State 42 (2000) 1207-1210.

M. Tetenbaum, Thermodynamic and Nonstoichiometric Behavior of Promising High-Tc Cuprate Systems via Electromotive Force Measurements: A Short Review, Metall. Mater. Trans. 30B (2000) 661-666.

S. P. Athur (Texas Center for Superconductivity), U. Balachandran and K. Salama (Texas Center for Superconductivity), Application of Melt Texturing to HTS Conductors, Advances in Cryogenic Engineering, Vol. 46B, pp. 887-894 (2000), eds. U. Balachandran, D. U. Gubser, K. T. Hartwig, and V. A. Bardos.

T. G. Truchan, F. N. Rountree, M. T. Lanagan, S. M. McClellan, D. J. Miller, K. C. Goretta; M. Tomsic (Eurus Technologies, Inc.); and R. Foley (IIT), Preparation of Nickel Substrates for Coated Conductors, Presented at 16th Intl. Conf. on Magnet Technology, Tallahassee, Sept. 26-Oct. 2, 1999; in IEEE Trans. Appl. Supercond. 10, 1130-1133 (2000).

Submitted

T. R. Askew (Kalamazoo College) and Y. S. Cha, Transient Response of 50-KiloAmp Y-123 Rings and Ring Pairs to Pulsed Magnetic Fields, Paper presented at Applied Superconductivity Conf. 2000, Virginia Beach, VA, Sept. 17-22, 2000.

S. Athur (Texas Center for Superconductivity); U. Balachandran; and K. Salama (Texas Center for Superconductivity), Fabrication of Yb-123 Tapes, Proc. Applied Superconductivity Conference 2000, Virginia Beach, VA, Sept. 17-22, 2000.

U. Balachandran, Development of High-Temperature Superconductors for Electric Power Applications, Presentation at State University of Sao Paulo at Ilha Solteira, Brazil, June 14, 2000.

U. Balachandran, High-Temperature Superconductors, Oral presentation at Associate Laboratory Director's Quarterly Meeting, Argonne, June 26, 2000.

U. Balachandran, The Accelerated Coated Conductor Initiative Strengthening the National Laboratories, Presentation at Industrial Overview Committee Meeting, Focus Session, Los Alamos, NM, Aug. 28-29, 2000.

U. Balachandran, Report to the Industrial Overview Committee for the Superconductivity Technology Centers, Presentation at Industrial Overview Committee Meeting, Los Alamos, NM, Aug. 28-29, 2000.

U. Balachandran and J. G. Daley (USDOE), Development of High-Temperature Superconductors for Electric Power Applications, Invited abstract presented at ICMC 2000: Superconductors for Applications, Material Properties and Devices, Rio de Janeiro, June 11-15, 2000.

Y. S. Cha and T. R. Askew (Kalamazoo College), Transient Characteristics of a High-T_c Superconductor Tube Subjected to Internal and External Magnetic Fields, Proc. Applied Superconductivity Conference 2000, Virginia Beach, VA, Sept. 17-22, 2000.

M. P. Chudzik, R. Koritala, Z. P. Luo, D. J. Miller, U. Balachandran; and C. R. Kannewurf (Northwestern U.), Mechanism and Processing Dependence of Biaxial Texture Development in Magnesium Oxide Thin Films Grown by Inclined-Substrate Deposition, Proc. Applied Superconductivity Conference 2000, Virginia Beach, VA, Sept. 17-22, 2000.

M. G. Ennis, T. J. Tobin (S&C Electric Co.); J. R. Hull, and Y. S. Cha, Fault Current Limiter - Predominantly Resistive Behavior of a BSCCO Shielded-Core Reactor, Proc. Applied Superconductivity Conference 2000, Virginia Beach, VA, Sept. 17-22, 2000.

Y. A. Jee, B. Ma, M. Li, B. L. Fisher, and U. Balachandran, Texture Formation and Superconducting Properties of $YBa_2Cu_3O_X$ Thin Films Prepared by a Solution Process on $LaAlO_3$ Single Crystals, Abstract to be presented at the Materials Research Society Fall Mtg., Boston, Nov. 27-Dec. 1, 2000.

R. E. Koritala, M. P. Chudzik, U. Balachandran, Z. P. Luo, D. J. Miller; and C. R. Kannewurf (Northwestern U.), Transmission Electron Microscopy Investigation of Texture Development in Magnesium Oxide Buffer Layers, Proc. Applied Superconductivity Conference 2000, Virginia Beach, VA, Sept. 17-22, 2000.

M. Lelovic, R. Koritala, B. Fisher, U. Balachandran; N. Vo, V. Selvamanickam, and P. Haldar (IGC-SuperPower), Novel Technique for Improving Field Dependence in Bi-2223 Superconducting Tapes at 77 K, Proc. Applied Superconductivity Conference 2000, Virginia Beach, VA, Sept. 17-22, 2000.

M. Li, B. Ma, Y. A. Jee, B. L. Fisher, and U. Balachandran, Structural and Electrical Properties of $YBa_2Cu_3O_X$ Thin Films on Biaxially Textured Buffered Ni-Based Alloy Substrates, Abstract submitted to the Materials Research Society Fall Meeting, Boston, Nov. 27-Dec. 1, 2000.

T. M. Mulcahy, J. R. Hull, K. L. Uherka; R. A. Abboud, and J. Juna (UNICOM), Test Results of 2-kWh Flywheel Using Passive PM and HTS Bearings, Proc. Applied Superconductivity Conference 2000, Virginia Beach, VA, Sept. 17-22, 2000; to be published in IEEE Trans. Appl. Supercond. 11 (2001).

B. C. Prorok, J.-H. Park, K. C. Goretta, R. E. Koritala, U. Balachandran; and M. J. McNallan (U. of Illinois at Chicago), Internally Oxidized Ag/1.2 at.% Mg Sheaths for Bi-2223 Tapes, Proc. Applied Superconductivity Conference 2000, Virginia Beach, VA, Sept. 17-22, 2000.

V. Selvamanickam, G. Carota, M. Funk, N. Vo, P. Haldar (IGC-SuperPower); U. Balachandran, M. Chudzik; P. Arendt, J. R. Groves, R. DePaula, and B. Newnam (LASL), High-Current Y-Ba-Cu-O-Coated Conductor Using Metal Organic Chemical-Vapor Deposition and Ion-Beam-Assisted Deposition, Proc. Applied Superconductivity Conference 2000, Virginia Beach, VA, Sept. 17-22, 2000.

V. Selvamanickam, G. Carota, N. Vo, C. Trautwein, P. Haldar (IGC); U. Balachandran, M. Chudzik; P. Arendt, J. Y. Coulter, and B. Newnam (LASL), Y-123-Coated Conductor Fabrication Using IBAD and MOCVD, Abstract presented at Applied Superconductivity Conf., ASC 2000, Virginia Beach, Sept. 17-22, 2000.

U. P. Trociewitz, P. R. Sahm (Florida State U.); R. E. Koritala; L. Brandao, C. Bacaltchuk, and J. Schwartz (Florida State U.), Microstructural Development and Superconducting Properties of BaO_2-Added $Bi_2Sr_2CaCu_2O_{8+x}$, Proc. Applied Superconductivity Conference 2000, Virginia Beach, VA, Sept. 17-22, 2000.

T. G. Truchan, M. P. Chudzik, B. L. Fisher, R. A. Erck, K. C. Goretta, and U. Balachandran, Effect of Ion-Beam Parameters on In-Plane Texture of Yttria-Stabilized Zirconia Thin Films, Proc. Applied Superconductivity Conference 2000, Virginia Beach, VA, Sept. 17-22, 2000.

1998–2000 Patents

Method and apparatus for measuring gravitational acceleration utilizing a high temperature superconducting bearing
John R. Hull
U.S. Patent 6,079,267 (June 27, 2000).

Engineered flux pinning centers in BSCCO, TBCCO and Y-123 superconductors
Kenneth C. Goretta, Michael T. Lanagan, Jieguang Hu, Dean J. Miller, Suvankar Sengupta, John C. Parker, U. Balachandran, Donglu Shi, and Richard W. Siegel
U.S. Patent 5,929,001 (July 27, 1999).

Passive fault current limiting device
Daniel J. Evans and Yung S. Cha
U.S. Patent 5,892,644 (April 6, 1999).

Automatic HTS force measurement instrument
Scott T. Sanders and Ralph C. Niemann
U.S. Patent 5,889,397 (March 30, 1999).

Method and etchant to join Ag-clad BSCCO superconducting tape
Uthamalingam Balachandran, A. N. Iyer, and J. Y. Huang
U.S. Patent 5,882,536 (March 16, 1999).

Elongated Bi-based superconductors made by freeze dried conducting powders
Uthamalingam Balachandran, Milan Lelovic, and Nicholas G. Eror
U.S. Patent 5,874,384 (Feb. 23, 1999).

Thin-film seeds for melt processing textured superconductors for practical applications
Boyd W. Veal, Arvydas Paulikas, Uthamalingam Balachandran, and Wei Zhong
U.S. Patent 5,869,431 (Feb. 9, 1999).

Superconductor composite
Stephen E. Dorris, Dominick A. Burlone, and Carol W. Morgan
U.S. Patent 5,866,515 (Feb. 2, 1999).

Surface texturing of superconductors by controlled oxygen pressure
Nan Chen, Kenneth C. Goretta, and Stephen E. Dorris
U.S. Patent 5,856,277 (Jan. 5, 1999).

Method for synthesizing and sinter–forging Bi–Sr–Ca–Cu–O superconducting bars
Nan Chen, Kenneth C. Goretta, and Michael T. Lanagan
U.S. Patent 5,821,201 (Oct. 13, 1998).

Mixed-mu superconducting bearings
John R. Hull and Thomas M. Mulcahy
U.S. Patent 5,722,303 (March 3, 1998).